JGR Atmospheres

RESEARCH ARTICLE
10.1029/2025JD045131

Urban Land Surface Effects on Summertime Clouds and Moist Convection in Houston Under Different Synoptic Conditions

Ye Liu[1], Yun Qian[1], Colleen M. Kaul[1], Brian J. Gaudet[1], Larry K. Berg[1], Zhe Feng[1], Adam C. Varble[1], Sheng-Lun Tai[1], Ya-Chien Feng[1], Zhao Yang[1], T. C. Chakraborty[1], and Jerome D. Fast[1]

[1]Pacific Northwest National Laboratory, Richland, WA, USA

Key Points:

- Houston's urban surface increases summer cloud cover and convective activity, especially under weak synoptic conditions
- Urban heating drives moisture convergence and updrafts that enhance cloud depth, convective intensity, and rainfall near the city
- Dominant urban effects vary by synoptic regime, generally mechanical under strong meteorological forcing and thermodynamics under weak forcing

Correspondence to:

Y. Liu and Y. Qian,
ye.liu@pnnl.gov;
yun.qian@pnnl.gov

Citation:

Liu, Y., Qian, Y., Kaul, C. M., Gaudet, B. J., Berg, L. K., Feng, Z., et al. (2026). Urban land surface effects on summertime clouds and moist convection in Houston under different synoptic conditions. *Journal of Geophysical Research: Atmospheres*, *131*, e2025JD045131. https://doi.org/10.1029/2025JD045131

Received 21 AUG 2025
Accepted 24 MAR 2026

Abstract Urban landscapes modify cloud formation and convection through complex thermodynamic and aerodynamic processes; however, their influence under different synoptic regimes remains poorly understood. This study investigates the impact of the Houston metropolitan area on summertime cloud cover and convective cell characteristics using a combination of satellite observations, radar data, and high-resolution process-based modeling. We isolate urban effects by comparing model simulations with realistic urban land cover against hypothetical scenarios where all urban areas are replaced by rural vegetation. Results reveal that Houston's land cover consistently enhances cloud fraction and convective activity relative to surrounding rural areas, altered by large-scale meteorological forcing. Under weakly forced conditions, enhanced surface heat flux primarily contributes to driving low-level convergence and vertical ascent, leading to over 8% cloud fraction increase between 2 and 6 km over the city. Under strongly forced conditions, urban influences manifest differently depending on cloud type. For non-convective clouds, the city acts as a barrier that decelerates and lifts moist southerly inflow, increasing low cloud cover over the urban core, while decreasing it downwind the city. For convective clouds, both synoptic ascent and urbanization modulate moisture redistribution and cloud structure, producing modest cloud enhancement over the city and slight suppression over the downwind area. Urbanization exerts small changes in the intensity of the convective cells; however, it significantly decreases their duration and traveling distance. This work highlights the importance of accounting for land surface heterogeneity in modeling clouds and precipitation and demonstrates that urban impacts on clouds are highly regime-dependent.

Plain Language Summary Urban areas can change local weather by modifying heat, moisture, and wind patterns. This study explores how Houston affects cloud formation in summer. Using satellite and radar data with high-resolution weather model simulations, the research compares the current Houston landscape to a version where the city is replaced by natural land cover. The goal is to understand how the combined effects of buildings, roads, and heat from the city surface change clouds under different weather conditions. Houston increases cloud cover and convective activity, especially on calm days with little large-scale weather influence. Heat from the city warms the air, drawing moisture from nearby rural areas. This moisture is lifted over the city, forming taller clouds and triggering storms that are stronger, longer lasting, and produce more rainfall than in rural areas. On days with strong winds or passing systems, the urban effect is smaller but noticeable, as buildings block or redirect winds. The effect depends on the time of day, with the largest impact on the afternoon. These findings highlight the need to consider urbanization in weather prediction. Future work will explore how building designs and surfaces can help manage these impacts.

1. Introduction

Urban areas are known to modify local and regional atmospheric processes through their distinctive surface characteristics (e.g., Yun Qian et al., 2022). Urbanization alters surface energy and water balances and generally enhances surface roughness, which can modify boundary-layer temperature, humidity, and winds (e.g., Barlow, 2014; Omidvar et al., 2020; Pielke, 2001; H. Zhang et al., 2019). A prominent outcome of urbanization is the urban heat island (UHI) effect, where urban areas are warmer than their rural surroundings, especially at night. These thermal and mechanical perturbations can influence cloud formation and precipitation (e.g., Katzfey et al., 2024; Liu et al,. 2022; Theeuwes et al., 2019). For example, METROMEX, an early field experiment on urban effects conducted in St. Louis, Missouri in the 1970s, provided empirical evidence of urban rainfall enhancement, finding 10%–17% more precipitation downwind of the city (Changnon et al., 1971). Numerous urban studies since then have strengthened this understanding of urban effect on precipitation as reviewed by Shepherd (2005). For instance, modeling studies have documented that urban-induced convergence and uplift can enhance thunderstorm development over and downwind of cities (e.g., Ashley et al., 2012; W. Zhang et al., 2018). Qian et al. (2022) extensively reviewed the urban impact on clouds and precipitation, highlighting the competing effects of urban heat island and urban dry island, which describes the tendency for urban areas to be warmer and drier than surrounding rural areas, on precipitation enhancement. A comprehensive meta-analysis of 85 studies by Liu and Niyogi (2019) found that urban areas on average increase precipitation by ∼16% over the city center and ∼18% downwind, with detectable changes extending tens of kilometers from the city, underscoring the need for a better understanding of the underlying processes.

While the influence of urbanization on precipitation has been widely recognized, fewer studies have focused specifically on how cities affect cloud cover, especially under varying meteorological conditions (Yun Qian et al., 2022; Theeuwes et al., 2019, 2022). Cloud formation modulates radiative budgets and temperatures in urban areas. Understanding cloud responses to urban land surface heterogeneity is challenging because cloud responses are modulated by meteorology (Rieck et al., 2014; Vo et al., 2023).

Houston, Texas is a large coastal metropolis that provides a compelling natural laboratory for studying urban effects on clouds and convection. This region is influenced by sea- and bay-breeze circulations, abundant Gulf of Mexico moisture, the Great Plains low-level jet (GPLLJ), and occasional frontal intrusions (e.g., Algarra et al., 2018; Y. Liu et al., 2024; Whiteman et al., 1997; Wu & Raman, 1996). These meteorological drivers lead to both weakly forced convective events triggered by diurnal heating and sea-breeze convergence and strongly forced convective events governed by fronts or upper-level disturbances (Chen et al., 2011; Wang et al., 2022). Climatological studies over southeastern Texas have shown that deep convection can initiate across a wide range of large-scale environments, from favorable patterns with frontal systems and low-level moisture convergence to unfavorable anticyclonic patterns with limited large-scale lift, where convection relies more on local forcing (Y. Liu et al., 2024; Song et al., 2019; Wang et al., 2022). Urban effects may be the most pronounced under weakly forced conditions, as the absence of a strong synoptic environment allows the urban-induced thermodynamic and aerodynamic influences to play a dominant role. For example, Mejia et al. (2024) utilized 900-m resolution simulations of the August 2020 heatwave to demonstrate that urban sensible heating and enhanced drag are the primary drivers of shallow cumulus formation under quiescent conditions. Furthermore, Mejia et al. (2024) highlighted the sensitivity of these clouds to surface energy changes, showing that heat mitigation strategies can suppress urban cloud formation.

In this study, we present a process-level analysis of how the Houston metropolitan area influences summertime cloud cover and convection. Distinct from past Houston studies that emphasized precipitation or aerosol impacts, our focus is on the total urban land surface effect (combining thermodynamic and aerodynamic influences of the city) on cloud fraction and precipitating convective cell characteristics over multiple summers under variable large-scale meteorological environments. We leverage satellite-derived cloud cover and radar data to establish the observed cloud and precipitating convection anomalies over the Houston metropolitan area. We then use convection-permitting model simulations for three summers (2020–2022) to isolate urban effects. We further stratify the analysis according to the large-scale meteorological patterns (LSMPs) to examine how urban effects vary by synoptic setup. Overall, this work addresses the following questions: (a) How does the Houston urban area affect the spatial distribution and diurnal cycle of cloud cover under summertime conditions? (b) What are the mechanisms by which the urban land surface alters low-level convergence, moisture transport, and convective development? (c) How do these urban effects differ between periods with strong and weak large-scale meteorological forcing?

2. Data and Methods

2.1. Study Region and Period

Our study focuses on the Houston metropolitan region in southeast Texas (approximately centered at 29.76°N, 95.37°W) and surrounding rural areas. Houston lies about 50 km inland from the Gulf of Mexico coastline (Figure 1). The broader landscape consists of flat coastal plains dominated by grasslands, croplands, and patches of forest. The region experiences a hot and humid climate during the boreal summer (June-July-August), making it favorable for convective cloud development.

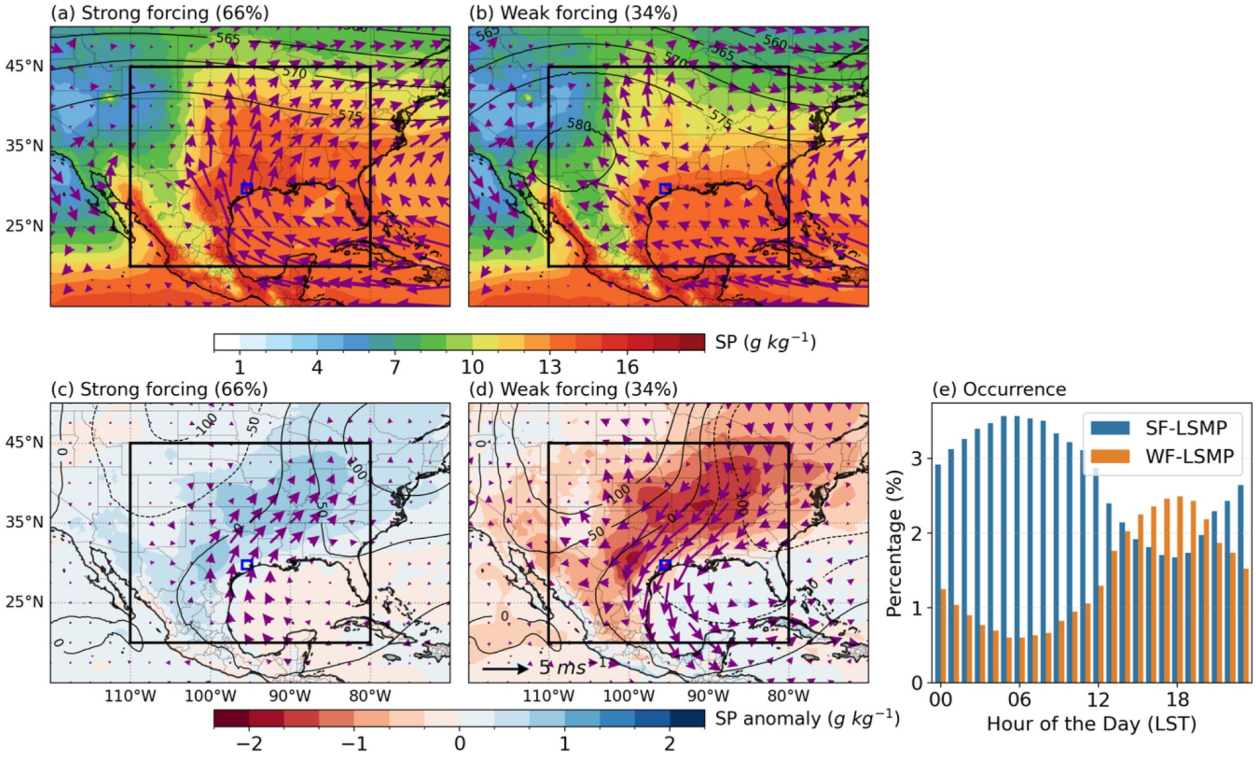

Figure 1. Wind vector (m s^{-1}), specific humidity at 925 hPa (shading, g kg^{-1}) and 500 hPa geopotential height (contour, gpm) under (a), (c) strongly and (b), (d) weakly forced large-scale meteorological patterns (LSMPs), and (e) the percentage occurrence of each LSMP as a function of the hour of the day. (a) and (b) are for the mean values, and (c) and (d) are the anomalies. Percentages in the parentheses on the maps indicate the frequency of each LSMP, the black boxes indicate the region used to identify the LSMP, and the blue boxes indicate the location of Houston. SF stands for strongly forced and WF stands for weakly forced.

Following Liu et al. (2024), we classified LSMPs by applying the Self-Organizing Map (SOM) (Vesanto & Alhoniemi, 2000) to horizontal wind components (u, v) and specific humidity (q) at 925 hPa from the fifth-generation European Centre for Medium-Range Weather Forecasts reanalysis (ERA5) (Hersbach et al., 2020) over the domain covering 28–32°N, 97–93°W. In this study, we group the four LSMPs defined by Liu et al. (2024) into two categories for simplicity: the pre-frontal and frontal LSMPs are classified as strongly forced LSMP, whereas the anti-cyclonic and weak anti-cyclonic LSMPs are categorized as weakly forced LSMP. These two categories align well with the four synoptic regimes (pre-trough, post-trough, anti-cyclonic, and transitional) identified over southeastern Texas by Wang et al. (2022). The strongly forced LSMP is associated with enhanced GPLLJ, facilitating robust northward transport of moist air from the Gulf water, as indicated by stronger southerly flow and higher specific humidity (Figures 1a and 1c), which either enhances new convection initiation or extends offshore clouds inland. In contrast, the weakly forced LSMP exhibits weaker southerly winds and reduced moisture advection into the Great Plains (Figures 1b and 1d), suggesting diminished moisture transport. Under this condition, deep convection initiation is commonly driven by local processes such as sea-breeze circulation, which arise from thermal contrasts between the land surface and Gulf waters.

Our analysis spans three summers in 2020, 2021, and 2022, offering a range of meteorological conditions. Of the total analyzed hours, 66% were influenced by strongly forced LSMP, while 34% were weakly forced (Figure 1). The diurnal distribution reveals a clear temporal separation between patterns. Strong forcing LSMP are most frequent during the late night and morning hours, while weak forcing LSMP predominates in afternoon in early evening.

2.2. Observational Data

We utilized satellite and radar observations to characterize cloud and precipitation patterns. Cloud cover data are derived from the Moderate Resolution Imaging Spectroradiometer (MODIS) Level-2 Cloud Product (MYD06_L2) aboard NASA's Aqua satellites for the summers of 2003–2021 (https://ladsweb.modaps.eosdis.na

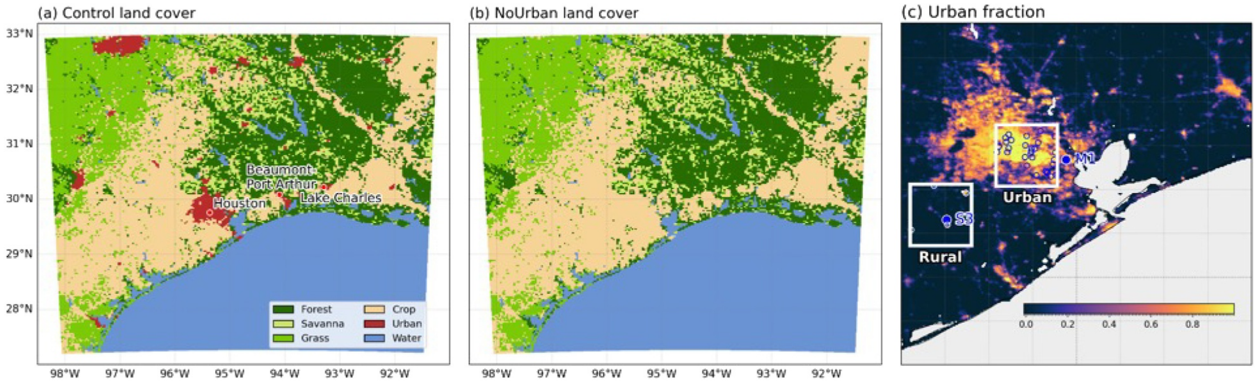

Figure 2. Land cover map used in (a) Control and (b) NoUrban experiments, and (c) urban fraction with blue dots indicating the location of radiosonde and the open circles indicating the MesoWest meteorological stations. Panel c zooms into the Houston metropolitan.

sa.gov/missions-and-measurements/products/MYD06_L2, last access 21 Dec 2025) (Platnick et a., 2015). The Aqua satellite overpass time is approximately 13:30 local time. Therefore, the derived cloud climatology represents conditions during the early afternoon, coinciding with the period of strong surface heating and sea-breeze development.

Precipitation patterns are examined using reflectivity observations from the Houston (KHGX) Next Generation Weather Radar (NEXRAD) for 2018–2022. The original Level-II reflectivity is obtained from Amazon Web Services (https://registry.opendata.aws/noaa-nexrad/, last access 21 May 2025) at approximately 5 min intervals and is interpolated from polar to Cartesian coordinates at 500 × 500 × 500 m ($x \times y \times z$) grid spacing using py-ART (Helmus & Collis, 2016) (https://arm-doe.github.io/pyart/, last access 21 May 2025). We focus on the frequency of heavy precipitation echoes (>30 dBZ) as a proxy for convective rainfall events.

To evaluate simulations, we obtain 2-m temperature data from MesoWest over the urban core (33 sites) and rural area (4 sites), as denoted by the white boxes in Figure 2c, which have similar distances to the coastline. MesoWest is a cooperative observational network designed to offer seamless access to both real-time and archived surface weather observations collected from federal and state agencies, universities, private networks, and citizen observers (https://mesowest.utah.edu/html/help/main_index.html, last access 22 June 2025). The original station measurements are aggregated to hourly means.

We use radiosonde data from the Tracing Aerosol Convection Interactions Experiment (TRACER) field campaign which occurred in 2022 (Jensen & PNNL, BNL, ANL, ORNL, 2023). The sounding data are obtained at the main site (M1, 29.67°N, 95.06°W) in La Porte near Galveston Bay and the ancillary site (S3, 29.32°N, 95.06°W) to the southwest of downtown Houston in a rural region (https://www.arm.gov/research/campaigns/amf2021tracer, last access 21 May 2025). The locations of the two sites are marked by blue dots in Figure 2c.

2.3. Model Configuration

To isolate the impact of urbanization on clouds, we conducted numerical simulations with the Weather Research and Forecasting (WRF) version 4.2 (Skamarock et al., 2019). The model domain is centered on Houston and covers southeastern Texas, 639 km × 660 km horizontal extent, with a horizontal grid spacing of 3 km to permit representation of convective cloud systems. The configuration includes 44 vertical levels with the model top set at 10,000 Pa. Land use was prescribed using the MODIS International Geosphere-Biosphere Program (IGBP) 21 categories land use type. Updated sea-surface temperature as used. The model physics parameterization includes Thompson microphysics scheme (Thompson et al., 2004, 2008), Rapid Radiative Transfer Model for Global Climate Models longwave and shortwave schemes (Iacono et al., 2008), the Mellor-Yamada-Janjic (MYJ) planetary boundary layer scheme (Janjić, 1990), and the Unified Noah land surface model (Chen & Dudhia, 2001). The cloud fraction in the model is analyzed using Xu and Randall (1996) parameterization, which determines the fractional coverage of cloud within each grid cell based on the local relative humidity and total cloud condensate mixing ratio. The calculation utilized a critical relative humidity to determine the threshold for cloud formation.

Table 1

Default Physical Parameters Used in the BEP/BEM for the Urban Land Cover

	Low-intensity residential	High-intensity residential	Commercial/industrial
Urban fraction	0.50	0.90	0.95
Building height range (m)	5.0–15.0	10.0–20.0	15.0–35.0
Anthropogenic heat (W m^{-2})	16.0	20.0	36.0
Albedo (roof/wall/road)	0.2/0.2/0.2	0.2/0.2/0.2	0.2/0.2/0.2
Emissivity (roof/wall/road)	0.90/0.90/0.95	0.90/0.90/0.95	0.90/0.90/0.95

We used an updated multi-layer urban building environment parametrization (BEP) model and a multilayer building energy model (BEM) to represent urban surface physics, including heat storage in buildings, anthropogenic heat flux, and momentum drag (Martilli et al., 2002; Salamanca et al., 2010). BEP represents the impact of buildings on resolved airflow by treating the urban surface as a 3D street canyon (Martilli et al., 2002). Instead of using a fixed roughness length, BEP dynamically reproduces the vertical profile of Reynolds stress and reduces turbulence intensity below the average roof height based on building geometry. BEM is coupled to BEP to simulate the generation of heat in buildings and the exchange of heat with the exterior flow (Salamanca et al., 2010). It accounts for heat diffusion through walls, roofs, and floors, natural ventilation, radiation exchange between indoor surfaces, and anthropogenic heat generation. To capture urban heterogeneity, we utilized three distinct urban land use categories defined by specific building height distributions (ranging from 5 to 35 m) and impervious surface fractions (ranging from 0.50 to 0.95), as defined in Table 1. The impact of urban-induced aerosols is not included in this study, although would be needed to more completely treat physics in this region for real-world conditions.

Two experiments were run for the summers of 2020–2022, covering a wide range of meteorological conditions. The Control simulation (referred to as Control) used current urban land cover, while the NoUrban simulation used identical initial and boundary conditions as those in Control, but all urban land use in the domain was replaced by natural land cover (Figure 2). Each urban grid cell was reassigned to the most dominant natural land cover type (within the cell or its immediate neighborhood cells if it was 100% urban). Each simulation was initialized at 00 UTC on May 29th and run continuously through August 31st with boundary conditions from the ERA5 (Hersbach et al., 2020). In both experiments, the initial soil moisture and temperature fields were derived from ERA5 reanalysis. As the relatively small model domain and frequent lateral boundary updates (3-hourly) from ERA5 were sufficient to constrain the large-scale environment, no nudging was applied. The Control minus NoUrban difference isolates changes in clouds and precipitating convection attributable to the Houston metropolitan area surface conditions via effects on associated surface heat fluxes and roughness.

2.4. Convective Cell Identification and Tracking

We applied the open-source Python Flexible Object Tracker (PyFLEXTRKR, available from https://github.com/FlexTRKR/PyFLEXTRKR, last access: 21 May 2025) algorithm (Zhe Feng et al., 2023) to identify and track convective cells from the WRF simulated radar reflectivity saved at 5 min intervals. Convective cells are identified in PyFLEXTRKR (Zhe Feng et al., 2022) using a minimum composite reflectivity threshold of 10 dBz to define coherent precipitation features for tracking. Within these features, convective cores are identified using a modified Steiner et al. (1995) algorithm, which classifies grid points as convective if the reflectivity intensity exceeds 55 dBz or if the reflectivity horizontal texture satisfies a background-dependent peakedness criteria (with a weak echo threshold of 15 dBz). Cells are tracked between successive times by advecting cell masks and assessing their overlap with cell masks at the following time. Minimum overlap fraction and multiple cell overlap dictate whether a cell is continuing its track, splitting, or merging.

3. Results

3.1. Observed Cloud Cover and Precipitation Enhancement Over Houston

Satellite and radar observations provide compelling evidence that urbanization modifies cloud and precipitation patterns (Figure 3). Long-term daytime MODIS observations of summertime cloud fraction over 2003–2021

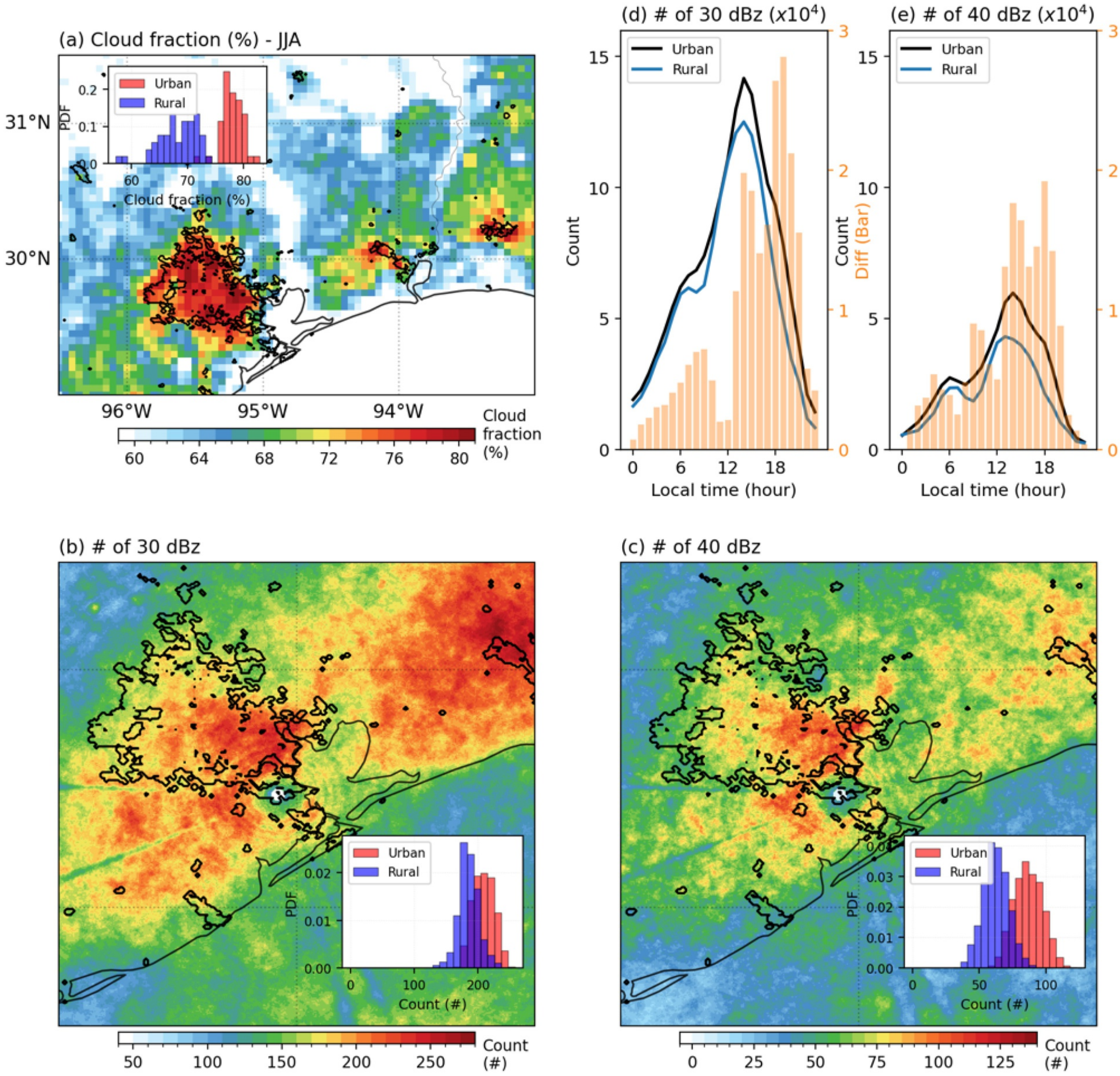

Figure 3. Observed cloud fraction (%) and number of grids reaching the radar reflectivity threshold. (a) Summer daytime MODIS Aqua (overpass time ~13:30 local time) cloud fraction in 2003–2021 over all weather pattern conditions. Number of points with radar reflectivity exceeding (b) 30 dBZ and (c) 40 dBZ at the KHGX site in 2018–2022 over all conditions. The black contours in (a) outline the locations of Houston, Beaumont, Port Arthur, and Lake Charles. (d) and (e) are the number of reflectivity exceeding the corresponding threshold at each hour with urban core and rural area denoted by the white rectangles in Figure 2c, with the lines indicating the numbers and the bars indicating the difference between urban and rural regions. The inserts in panels a, b, and c are the histograms of corresponding variables within the urban core and rural area as defined in Figure 2c.

reveal an inland enhancement relative to the adjacent Gulf waters. This urbanization-related cloud enhancement pattern aligns more clearly with the urban boundary when averaged over a longer period, while it shows up as patchy cloud enhancement over shorter periods (Mejia et al., 2024). Due to the afternoon overpass time, the cloud top height over the city area ranges in 4–7 km. This land-sea contrast in cloud cover is consistent with stronger daytime surface heating and sea-breeze-driven convergence over land, promoting inland afternoon cloud development (e.g., Mejia et al., 2024). Superimposed on the land-sea gradient, we observe a localized enhancement of cloud fraction over the Houston metropolitan area, Beaumont-Port Arthur area, and Lake Charles. The cloud cover over cities is 5%–10% higher than the surrounding rural land, with the enhancement spatially coherent with the urban boundary. It aligns with findings from other cities where satellites have noted higher cloud occurrence over urban areas (Theeuwes et al., 2022; Vo et al., 2023).

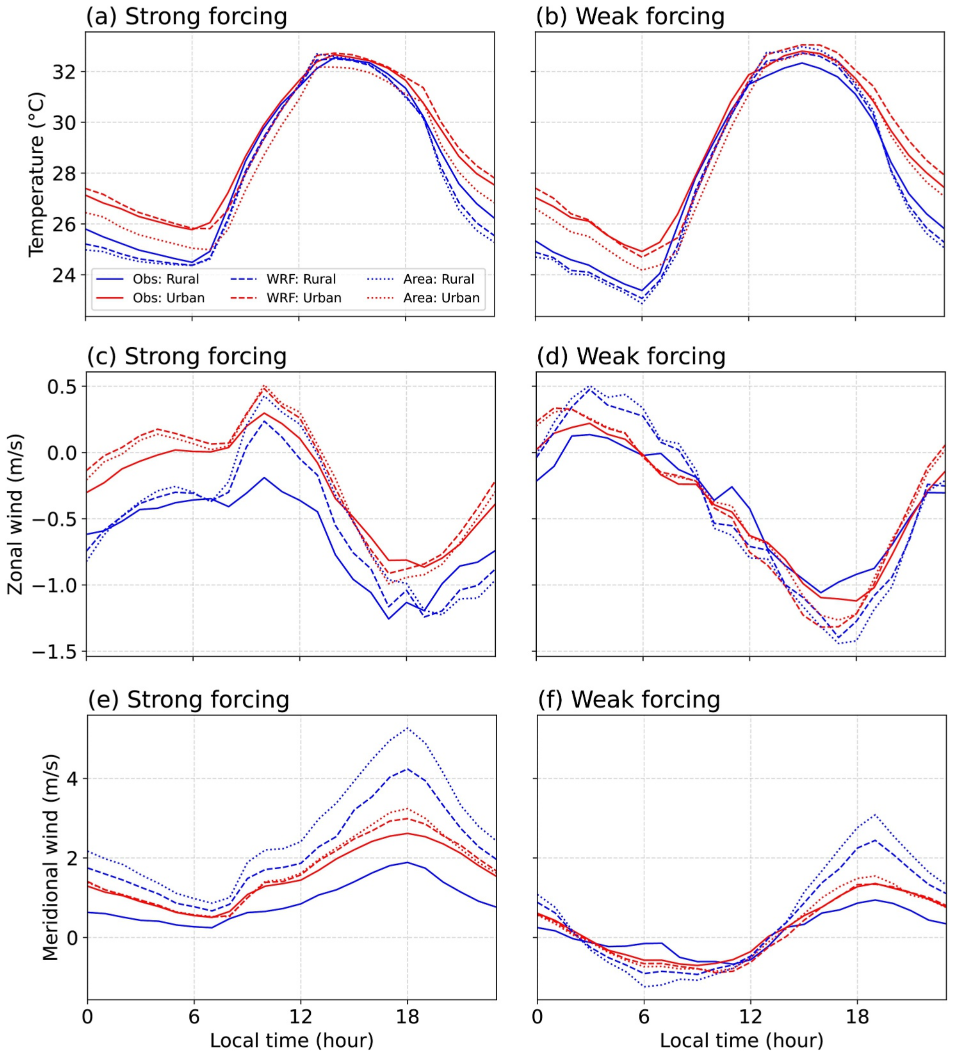

Figure 4. Diurnal variation of 2-m temperature (°C) and meridional and zonal wind speed (m s^{-1}) in observation and Control simulation during (a) strongly forced (SF) and (b) weakly forced (WF) large-scale meteorological patterns (LSMPs). The labels Obs and WRF indicate the average across the respective sites, while Area indicates the average over the urban core and rural area shown in Figure 2c.

The KHGX radar reflectivity analysis also reveals land and city enhancements. The number of occurrences of column maximum radar reflectivities exceeding 30 dBZ and 40 dBZ is higher over land, especially over urban areas, than over the adjacent Gulf waters (Figures 3b and 3c). Figures 3d and 3e show the diurnal cycle of moderate and heavy precipitation, comparing the frequencies of reflectivity values exceeding 30 and 40 dBZ between the urban core and nearby rural areas. Although both areas are similarly distant from the coast, the urban region consistently experiences more frequent precipitation, with maximum differences in the afternoon (13–18 LST or local standard time).

3.2. Model Evaluation Against Sounding Profiles

To evaluate the model performance in simulating the diurnal temperature cycle and urban heat island effect, we compare hourly 2-m temperature from WRF simulations with observations for both rural and urban locations during strongly forced and weakly forced periods (Figure 4). During the strongly forced period, the observed urban-rural temperature difference is 0.36°C during the daytime and 1.16°C at night, while the WRF Control simulation reasonably reproduces the diurnal pattern with values of 0.50°C during the day and 1.64°C at night. During the weakly forced period, the urban heat island effect is stronger, with observed (modeled) intensities of

0.56°C (0.45°C) during the daytime and 1.45°C (1.93°C) at night. This pronounced nocturnal UHI is driven by the large thermal storage capacity of the urban fabric. During the day, the urban canopy stores the solar energy, which is subsequentially released as longwave radiation into the boundary layer at night. This sustained heat release reduces the cooling rate over the city compared to the rapidly cooling rural surroundings (Qian et al., 2022). Overall, the model captures the magnitude and diurnal pattern of the UHI effect, though slightly overestimating the strength of UHI. We further extended the evaluation to include wind fields using diurnal surface composites. As shown in Figures 4c–4f, the model captures the diurnal variation of both zonal and meridional wind components. However, it tends to overestimate the meridional wind speed in both the strongly and weakly forced conditions, particularly over the rural area in the late afternoon. A similar overestimation of meridional winds in this region was reported by Mejia et al. (2024).

We further evaluate temperature, relative humidity (RH), and wind speed profiles with radiosonde observations from the TRACER field campaign collected at M1 (La Porte) and S3 (ancillary) sites (Figure 5). Observed profiles are derived from the soundings launched within ±3 hr of 00 UTC and 18 UTC. Simulated profiles from the WRF model are extracted at the nearest grid points corresponding to the sounding locations and matched to the dates and times of the radiosonde launches. The number of sounding profiles varies by location due to data availability. In the year 2022, during strongly forced periods, there are 43 profiles at S3 and 238 at M1; during weakly forced periods, 84 profiles are available at S3 and 163 at M1.

The Control simulation shows reasonably well agreement with observations. Near-surface temperatures are captured within approximately 0.5°C for both S3 and M1 sites across different LSMPs. Simulated lapse rates in the lower troposphere are consistent with observations, with mean values of around 0.6°C/100 m at M1 and 0.7°C/100 m at S3 during both strongly and weakly forced periods.

Despite M1 being considered an urban site during the TRACER field campaign, its close proximity to Galveston Bay results in slightly lower near-surface temperatures and higher relative humidity than at the rural S3 site during the afternoon to evening hours. This pattern is consistent with the lake-breeze effects and thermal moderation by the water body described by Chakraborty et al. (2023). Overall, the Control simulation reasonably captures near-surface RH, with a slight overestimation. However, a systematic dry bias is evident in the lower free troposphere (above ∼1,500 m) at both sites and under both LSMPs. This underestimation of mid-level moisture is a well-documented characteristic of WRF planetary boundary layer parameterizations, often attributed to deficiencies in representing vertical moisture entrainment across the boundary layer top (Labzovskii et al., 2018; Tymvios et al., 2018). The boundary-layer depth, marked by the sharp humidity decrease between 800 and 1,500 m a.g.l., varies by location, time, and LSMPs. During strongly forced periods, a sharper vertical gradient in RH is observed and both sites are compared to those during weakly forced periods. The Control simulation captures these differences in boundary layer structure between the two LSMPs.

Regarding the wind profile (Figure 5), the model accurately reproduces the low-level jet structure at 00 UTC. However, it tends to underestimate the afternoon wind speed between 100 and 1500 m at the S3 site under both strongly and weakly forced conditions. At the M1 site, this underestimation is observed at both 00 UTC and 18 UTC across both meteorological conditions. Despite these biases in wind speed magnitude, the model correctly captures the distinct shear environments essential for this study.

To assess the robustness of the simulated cloud fields, we compared the modeled column-maximum cloud fraction with the MODIS Level-2 cloud product (MYD06_L2). Figure 6 shows the spatial distributions of the mean cloud fraction (top) and the corresponding anomalies relative to the domain average (bottom) under strongly and weakly forced conditions, respectively. Overall, the model produces a lower cloud fraction than MODIS. This systematic bias in absolute magnitude likely reflects differences in the definition and sampling of cloud fraction between the model and satellite observations (e.g., Qian et al., 2012). For instance, MODIS cloud retrievals rely on a binary (0/1) cloud mask rather than a fractional cloud amount, which tends to overestimate partially cloudy scenes. In addition, off-nadir viewing geometry can capture cloud sides and thereby increase the apparent cloud coverage. In contrast, the model's representation of vertical cloud overlap—approximated here by the column-maximum cloud fraction—can lead to an underestimation of total cloudiness. Further discrepancies may arise from differences in temporal sampling (continuous model output vs. twice-daily satellite overpasses) and from differing cloud detection thresholds between satellite sensors and the model (e.g., relative-humidity-based criteria). Despite these differences, the model successfully reproduces the observed spatial patterns of

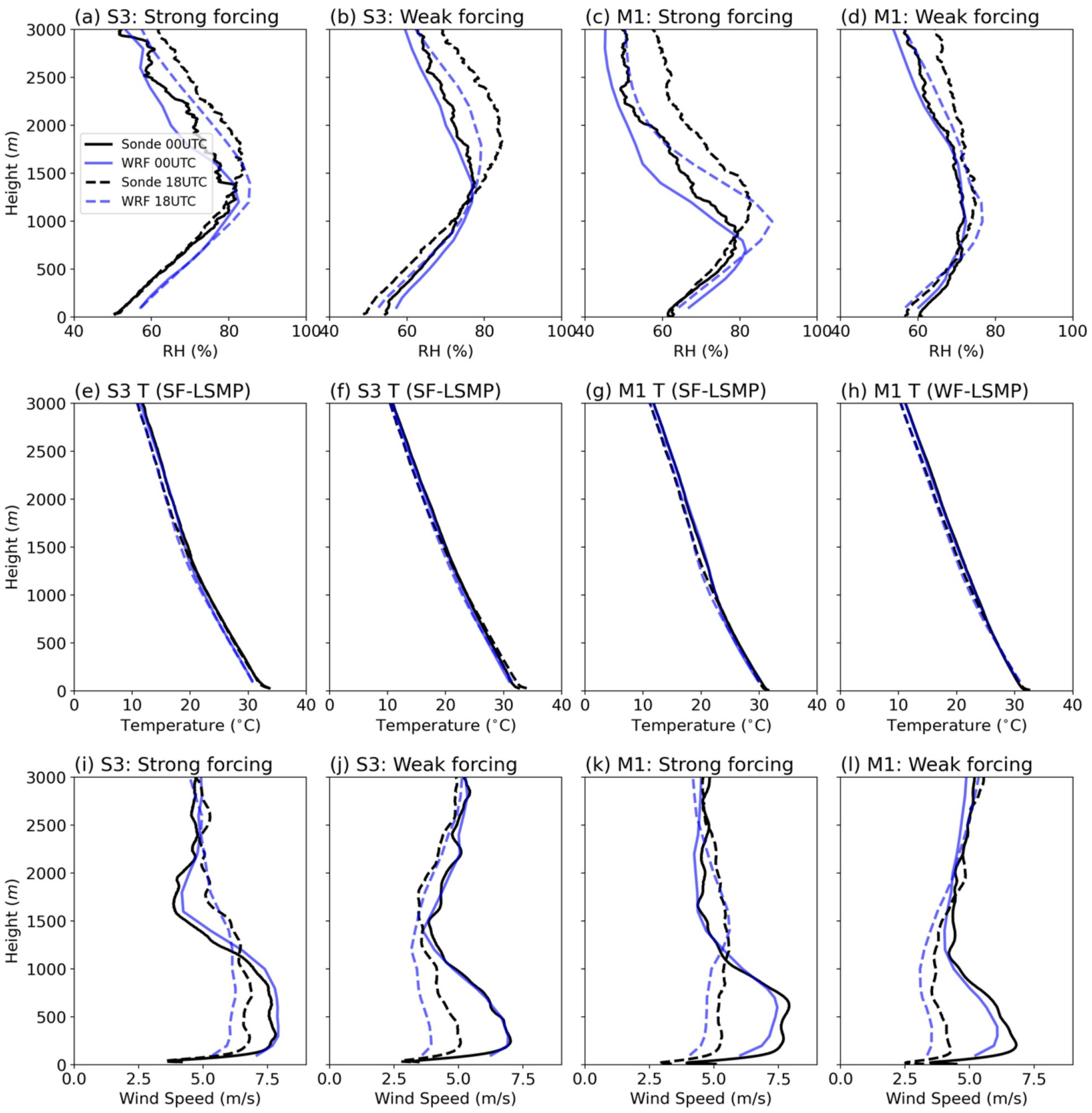

Figure 5. Mean profiles of temperature (T, °C), relative humidity (RH, %), and wind speed (Wind, m s^{-1}) in observation and Control simulation. M1 indicates the sounding location at La Porte and S3 indicates the ancillary site, as marked on Figure 2c.

cloud-fraction anomalies and the urban–rural contrast, lending confidence to its physical representation of urban impacts on cloud fields.

Overall, the WRF simulation with the chosen physical parameterizations captures the essential average thermodynamic characteristics of the Houston environment during the study period. Minor discrepancies in RH and boundary-layer structure fall within the typical uncertainty range reported for summertime convection-permitting simulations (e.g., Labzovskii et al., 2018; Tymvios et al., 2018). Having evaluated the base state, we examine the differences between the Control and NoUrban simulations to characterize urban impacts.

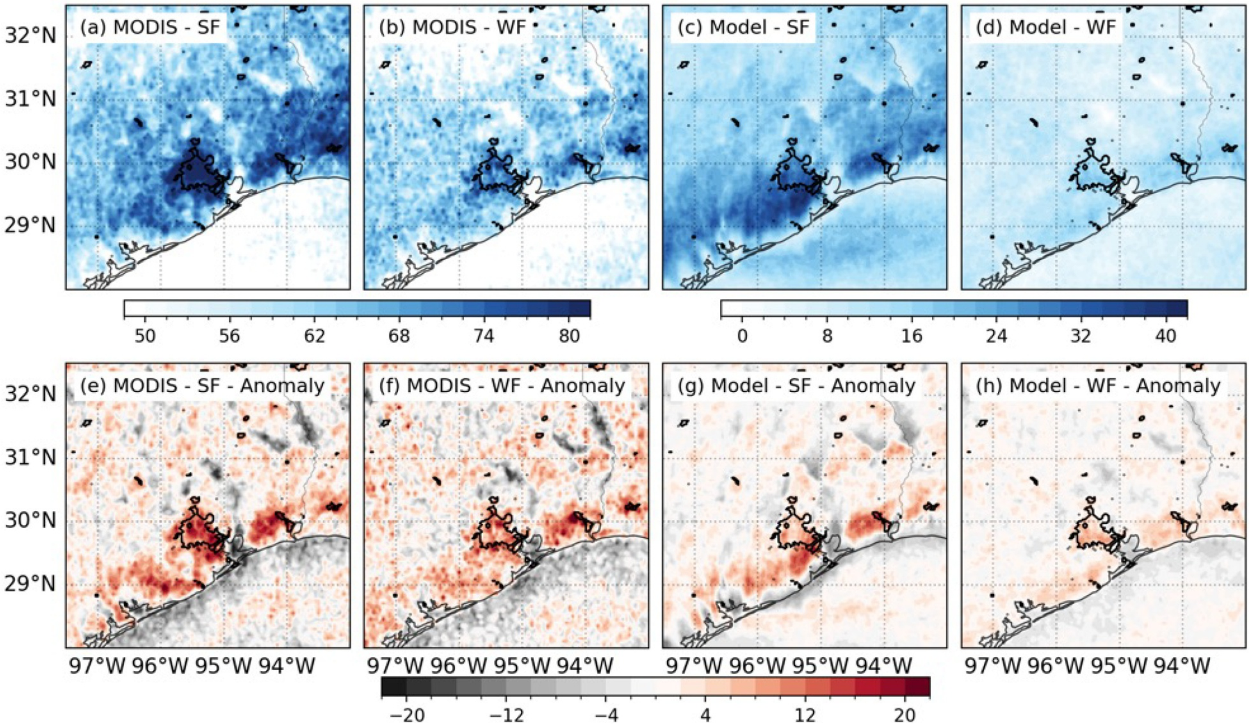

Figure 6. Comparison of daytime (~1300 LST) cloud fraction (%) from MODIS and control simulations. Panels (a–d) are mean cloud fraction and (e–h) are the anomalies with respect to the domain-wide average.

3.3. Cloud Cover Diurnal Cycle and Forcing-Regime Dependence

We explore how cloud cover evolves throughout the day in response to urbanization, and how this depends on the large-scale meteorological pattern, or LSMPs. Figure 7 provides time–height cross-sections of cloud fraction over the Houston urban core (averaged over the white box in Figure 2c) in Control simulation. Our analysis primarily focusses on the low levels between 200 m and 2 km and the middle level between 2 and 6 km. Averaging over all-weather conditions, the cloud fraction over the city exhibits a pronounced diurnal cycle. From midnight in early morning, there is a prevalence of low clouds between 500 m and 2 km, with cloud fraction around 3%–15%. The cloud fraction peak increases with height from morning to early afternoon as surface heating mixes and deepens the boundary layer, with low cloud cover decreasing through the afternoon after peaking in the late morning. In the afternoon (13–19 LST), deeper convective cloud form, with cloud bases lifting to 1 km and clouds reaching above 6 km. The cloud fraction in 2–6 km peaks at around 3%–8% at around 15 LST.

Comparing Control and NoUrban simulations, we find that the urbanization increases total cloud cover over Houston at most times of day (Figure 7d). Nighttime and early morning low cloud fractions are significantly increased in the Control simulation. Conversely, urbanization slightly reduces cloud fraction below 2 km around noon. In the afternoon, it increases the cloud fraction above 2 km, reflecting an increased convective potential associated with the UHI effect.

Under the strongly forced LSMP, the diurnal pattern broadly resembles the all-weather average but with overall larger low-cloud fractions. The urban effect induces a stronger enhancement of low clouds over night in early morning compared to the all-weather average. However, the afternoon enhancement between 2 and 6 km is more subtle. Under the weakly forced LSMP, cloud cover below 2 km is considerably reduced compared to the all-weather or strongly forced LSMP, with few clouds in the morning. Clouds start building up between 2 and 6 km in the afternoon and persists longer into the night compared to strong forcing conditions. The urban effect significantly increases cloud fraction in the middle levels between 13 and 19 LST.

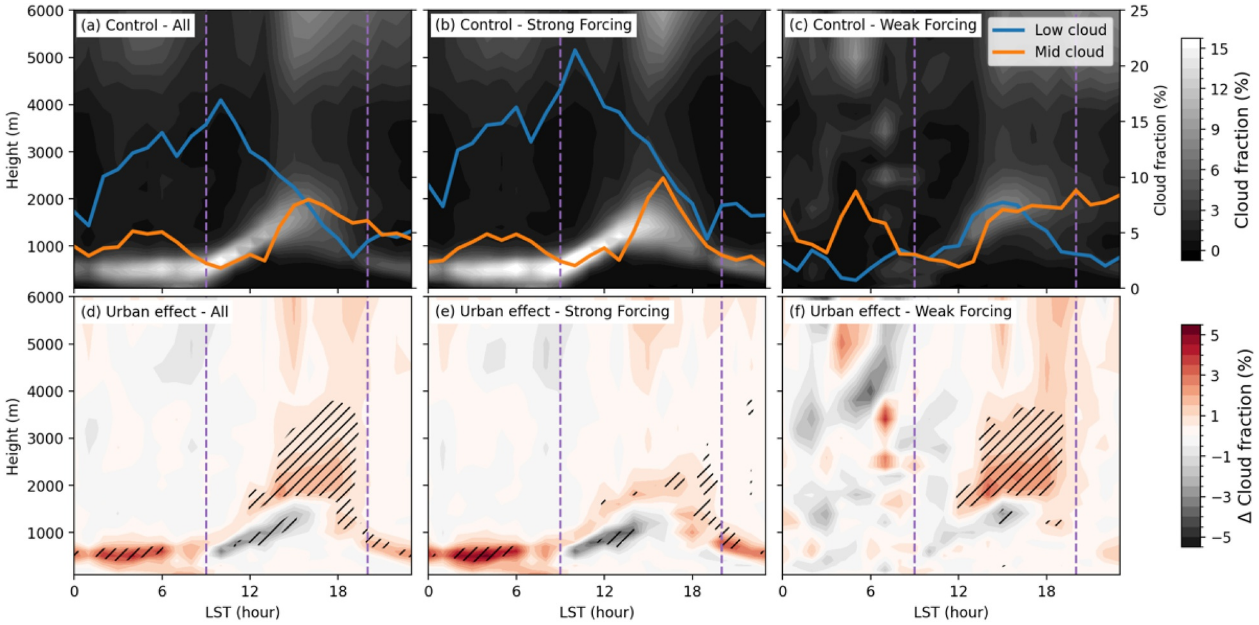

Figure 7. Time–height cross-sections of cloud fraction (%) over the Houston urban area, averaged over the white box in Figure 3c. (a)–(c) Control simulation and (d)–(f) difference between Control and NoUrban simulations, composited over (a), (d) all-data, (b), (e) the strongly forced large-scale meteorological pattern (LSMP), and (c), (f) the weakly forced LSMP. The purple vertical lines denote the hours at 09 LST and 20 LST. Hatched areas in (d)–(f) indicate differences statistically significant at the 95% confidence level using a Student's *t*-test.

3.4. Urban Effects on Cloud Spatial Patterns

Urbanization consistently enhances total cloud cover across all conditions examined, with its impact varying throughout the day and under different large-scale conditions. To isolate the underlying mechanisms, we focus on three representative regimes defined by combinations of LSMP and time window. The strongly forced morning (SFM) and afternoon (SFA) regime correspond to the early morning hours (00–06 LST) and afternoon (13–19 LST) under strongly forced LSMPs, respectively. The weakly forced afternoon (WFA) corresponds to 13–19 LST period under weakly forced LSMPs.

Figure 8 presents composites for cloud fraction in the low and middle levels during SFMs, WFAs, and SFAs. During SFMs, the Control simulation shows extensive low clouds offshore with some extending onshore in the prevailing southerly winds. Superimposed on this background, a localized cloud cover maximum is centered over Houston, with a relative minimum downwind (north) of the city (Figure 8a). Urbanization increases low cloud cover by up to 8% over the urban core and reduces it by 2%–5% downwind, but there is no significant impact on cloud cover in middle levels (Figures 8g and 8j), consistent with this being a non-convective pattern. The moisture flux differences during the same SFMs in Figure 9a indicate that the strong southerly wind is slightly decelerated over Houston and accelerated around its periphery.

To understand the mechanism behind these cloud changes, we evaluate composites for the surface energy budget and planetary boundary layer height (PBLH) (Figure 9) and the low-level moisture budget (Figure 10). Changes in downward shortwave and longwave radiation are small in all regimes no shown). During SFMs, urbanization only modestly perturbs surface sensible and latent heat fluxes, but it deepens the PBL over Houston and reduces PBLH over a broader area to the north (Figures 9a, 9d and 9j). Differences in low-level moisture flux show that the strong southerly flow is slightly decelerated over the city and accelerated around its periphery (Figure 10a). This deflection produces enhanced moisture flux convergence south of Houston and divergence to the north (Figure 10d). Decomposing moisture flux convergence ($-\nabla \cdot (qV)$) into mass convergence ($-q\nabla \cdot V$) and advection ($-V \cdot \nabla q$) terms reveals that the anomalies during SFMs are dominated by changes the mass convergence term (Figure 10h). While this term depends on both specific humidity and wind divergence, the fractional changes in urban-induced flow divergence are an order of magnitude larger than the fractional changes in moisture. Therefore, the moisture surplus is primarily driven by the mechanical modification of the wind field rather than the moisture gradient. Therefore, in this regime, the city primarily acts as an obstacle to modify the

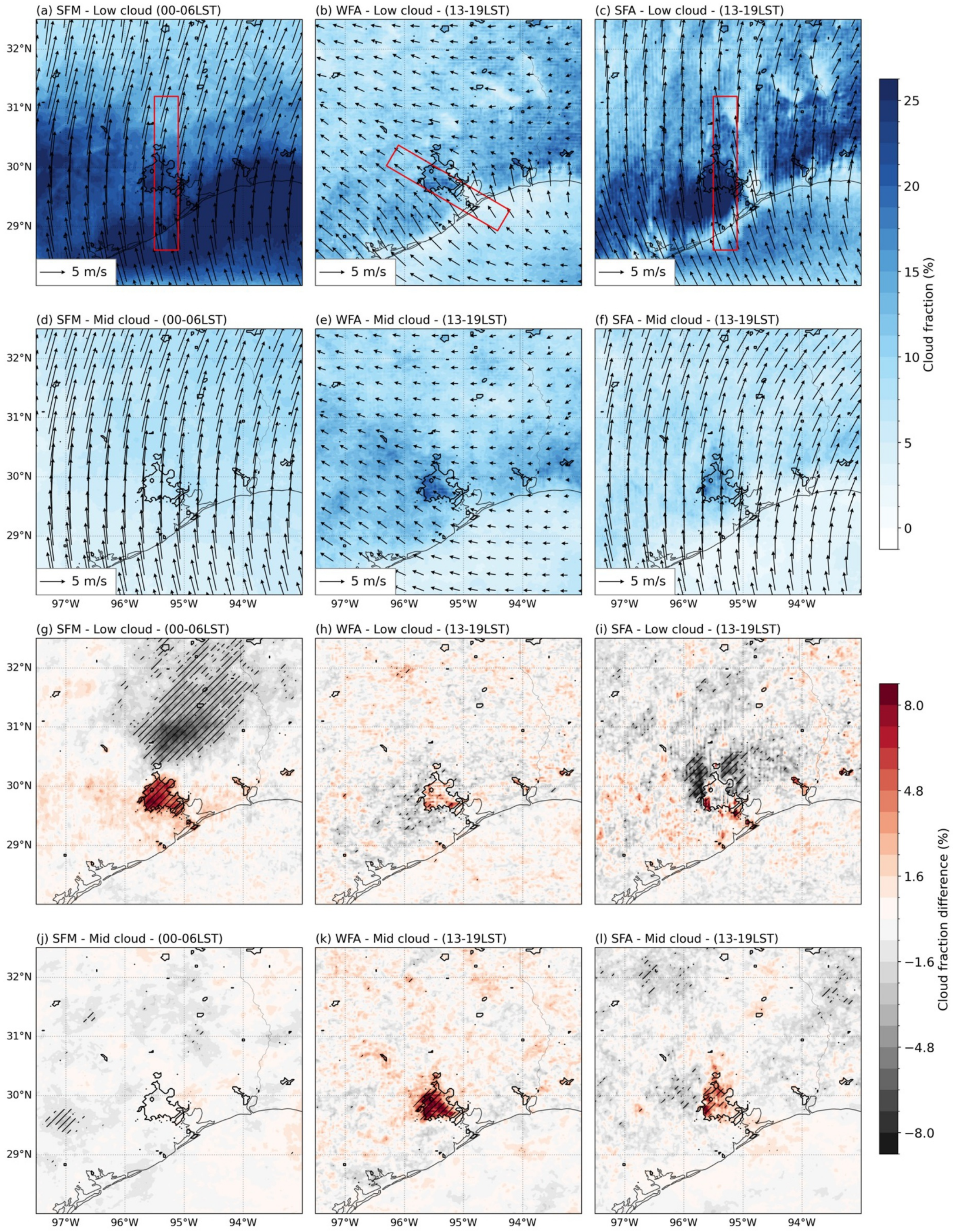

Figure 8. Spatial distribution of cloud fraction (%) and wind vector (m s^{-1}) for (a–f) the Control simulation and (g–l) corresponding differences between the Control and NoUrban simulations. Results are composited for strongly forced morning (SFM; 00–06 LST), weakly forced afternoon (WFA; 13–19 LST), and strongly forced afternoon (SFA; 13–19 LST) regimes. Hatched areas in (g–l) indicate statistically significant differences at the 95% confidence level. The red rectangles in (a–c) indicate the regions for cross-section calculation.

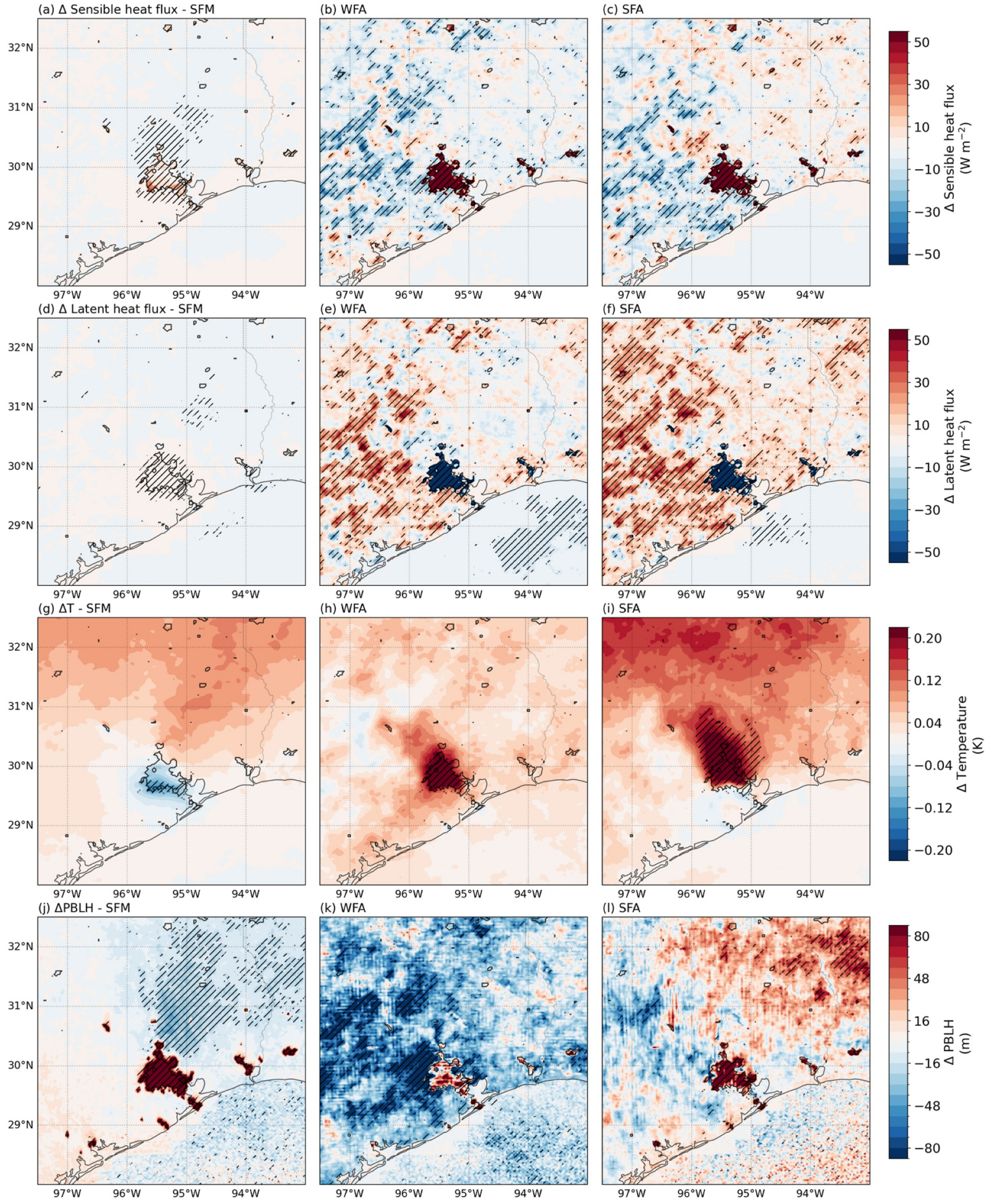

Figure 9. Urban effect (Control–NoUrban) on sensible heat flux (W m^{-2}), latent heat flux (W m^{-2}), 0–2,000 m mean air temperature (T, K), and planetary boundary layer height (PBLH, m). Hatched areas indicate statistically significant differences at the 95% confidence level according to a Student's *t*-test. SFM stands for strongly forced morning (00–06 LST), WFA stands for weakly forced afternoon (13–19 LST), and SFA stands for strongly forced afternoon (13–19 LST).

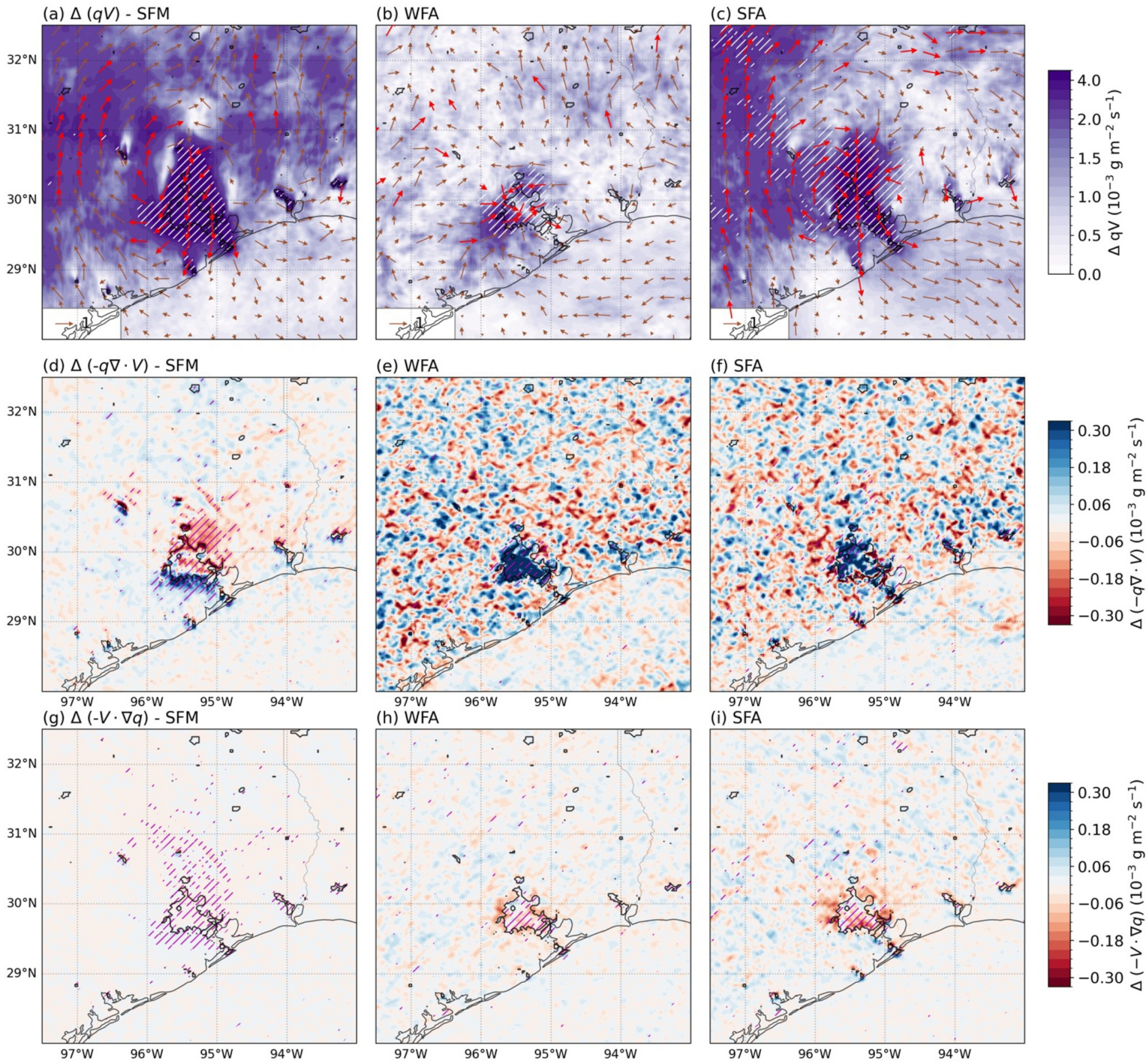

Figure 10. Urban effect (Control–NoUrban) on low-level moisture flux (10^{-3} g m^{-2} s^{-1}), moisture convergence (10^{-3} g m^{-3} s^{-1}), and advection (10^{-3} g m^{-3} s^{-1}) integrated from the surface to 2000 m. Vectors in (a–c) are horizontal moisture flux. Red vectors denote the significant values either in zonal or meridional components at 95% confidence level. Hatched areas indicate statistically significant differences at the 95% confidence level according to a Student's *t*-test. SFM stands for strongly forced morning (00–06 LST), WFA stands for weakly forced afternoon (13–19 LST), and SFA stands for strongly forced afternoon (13–19 LST).

existing marine-layer cloud by slowing the moist airflow, forcing some of it to rise (discussed further in Section 3.5) and some of it to divert around the city, resulting in less moisture immediately downwind.

During WFAs, the Control simulation shows a sea-breeze passing over Houston (Figure 8b). Relative to SFM conditions, the cloud field is patchier, with more clouds over land, and clouds extending from low to middle levels. Urbanization increases the cloud fraction over the city in both low and middle levels, with an increase in the middle level clouds exceeding 8% (Figures 8h and 8k). Urbanization significantly increases sensible heat flux and decreases latent heat flux over the city, thus increasing the Bowen ratio (Figures 9b and 9e). The moisture flux responses exhibit a nearly symmetric inflow toward Houston, as moist air from surrounding rural areas converges over the urban core (Figure 10b), primarily driven by increased moisture convergence (Figures 10e and 10h). This pattern reflects a typical UHI-induced circulation. Enhanced sensible heat flux deepens the PBL (Figure 9k) and draws in moist rural air that converges and forces vertical motion that triggers local cloud formation (e.g., Garuma, 2022; Mejia et al., 2024; Theeuwes et al., 2022). Outside the urban area, we find significantly decreased sensible heat flux and increased latent heat flux over the cropland west of Houston, while no significant changes occur over the forest region in the east. Given the absence of notable deviations in net radiation or precipitation over these areas, we hypothesize that this response is driven by the advection of urban heat. We propose that the urban-induced warming of the lower atmosphere (Figure 9h) enhances evaporative demand. Over the croplands, this likely stimulates transpiration due to lower stomatal resistance, leading to the observed evaporative cooling and reduced Bowen ratio. The muted response over the eastern forests suggests that the higher stomatal resistance and aerodynamic roughness of the forest canopy limit its physiological sensitivity to this advected atmospheric warming. Further sensitivity experiments focusing on plant physiological parameters are required to definitively isolate this mechanism.

During SFAs, when the strongly forced convective LSMP coincides with the daytime convective window, the Control simulation exhibits a widespread low cloud and cumulus towers reaching middle levels over the urban area (Figures 8c and 8f). The urban land cover effect on clouds also resembles a hybrid of the SFM and WFA conditions (Figures 8i and 8l). Cloud cover at low levels increases slightly along the southern edge of the city but decreases immediate downwind in rural areas, consistent with the upwind convergence and downwind divergence seen in SFM conditions. However, these effects are spatially constrained within ∼50 km north of Houston. Meanwhile, mid-level enhancement is centered over the urban area, closely resembling the WFA pattern. Together with increased sensible heat flux, decreased latent heat flux, and a deeper PBL over the city (Figures 9c–9f and 9l), this mixed spatial and vertical structure suggests that both synoptic lifting and UHI-induced buoyancy and convergence contribute to cloud enhancement over the city.

The above diagnostics also allow us to conceptually separate local and non-local contributions to the cloud response over Houston. The largest anomalies in low- and mid-level cloud fractions, PBL heights, sensible heat fluxes, and $-q\nabla \cdot V$ are tightly collocated with the urban core, indicating that local effects of the urban land cover (enhanced sensible heating, deeper PBLs, and UHI-induced low-level convergence and uplift) are the primary drivers of the increased cloud fraction directly above Houston. In contrast, cropland and grassland areas west of the city and forests to the east exhibit broader but weaker changes in precipitation and surface flux partitioning, which might slightly feed back to the atmosphere above the city.

Our finding that the urban heat island is the primary driver of cloud enhancement under weak synoptic forcing is consistent with the recent conclusions of Mejia et al. (2024) and Mejia et al. (2024), who identified thermal effects as the dominant mechanism over frictional convergence in similar quiescent environments. However, our analysis reveals that under strongly forced conditions, the mechanical drag of the urban canopy plays an increasingly important role in focusing moisture convergence, suggesting that the dominant urban mechanism is state-dependent.

3.5. Vertical Moisture Flux Convergence

To diagnose the mechanisms responsible for the cloud responses shown in previous sections, we analyze the vertical structure of moisture transport in the Control and NoUrban simulations. Figure 11 shows vertical cross-sections of specific humidity moisture fluxes and cloud fraction along the predominant wind direction, following the transects shown in Figure 8. These composites capture how the urban surface modulates moisture and subsequently influences cloud formation across three synoptic regimes.

During SFMs, shallow clouds originate over the Gulf water and are advected inland by southerly winds along with moist air. Upon encountering the urban surface, the flow decelerates and ascends along the southern edge of the city (Figure 11a). This mechanically induced uplifting elevates moisture to approximately 500 m, enhancing the cloud fraction over the urban area. In contrast, subsidence and horizontal moisture divergence occur north of the city and further downwind over rural regions, suppressing low-level cloud development (Figure 11b). This vertical structure is consistent with the dipole pattern seen in Figure 8g, with increased low clouds over the city and reduced coverage downwind.

During WFAs, the Control simulation shows a strong updraft over Houston, extending up to 2–3 km (Figure 11c). This vertical motion lifts moisture from the boundary layer, initiating cloud formation around 1.5 km above the city. Compared to SFM conditions, near-surface specific humidity is generally lower with inward moisture flux from surrounding rural areas (Figure 11d). The resulting low-level inflow converges over the urban core, consistent with Figure 8e, forming a vertically extended plume of elevated moisture enhanced cloud fraction above 1.8 km.

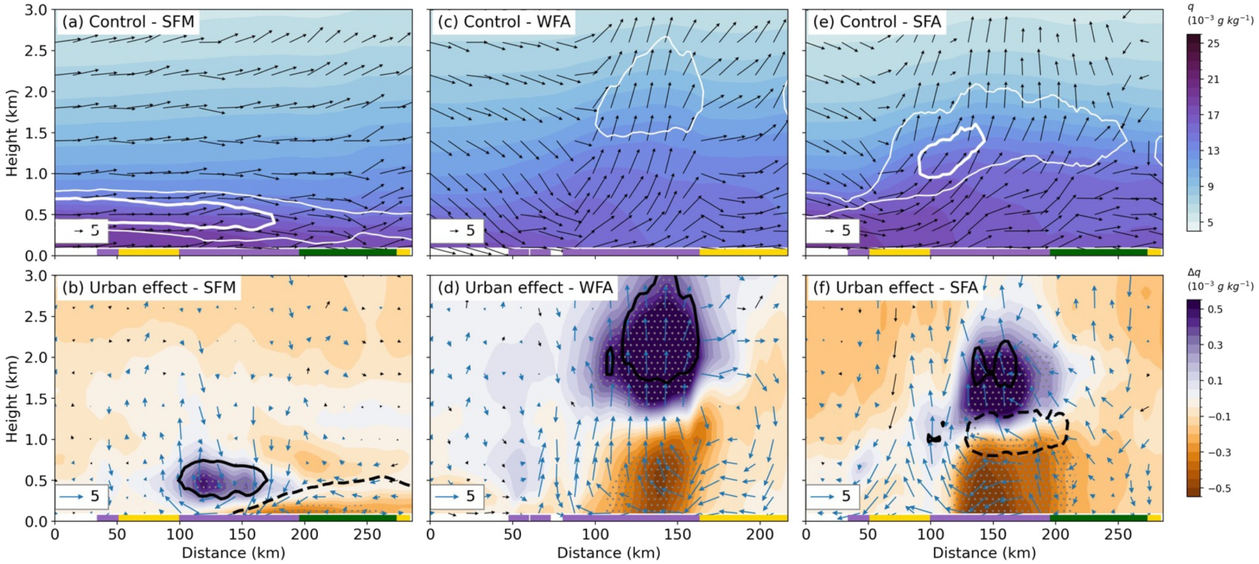

Figure 11. Cross-section of specific humidity (10^{-2} g kg^{-1}, shading), moisture flux (10^{-3} g m^{-2} s^{-1}, vector), and cloud fraction (5% thin and 10% thick contours in (a, c, e), and 5% solid and −5% dash contours in (b, d, f). Each cross-section is computed by averaging data along transects aligned with the prevailing wind direction, as defined by the red rectangles in Figure 8. Blue vectors indicate moisture flux differences that are statistically significant at the 95% confidence level. SFM stands for strongly forced morning (00–06 LST), WFA stands for weakly forced afternoon (13–19 LST), and SFA stands for strongly forced afternoon (13–19 LST).

The vertical structure during SFAs exhibits a hybrid signature combining elements of both SFM and WFA signatures. Synoptical scale transport (Figure 11e) delivers abundant low-level moisture, while urban heating enhances moisture convergence and ascent. As a result, urbanization dilutes and reduces moisture below 1 km over much of the city by enhanced lifting, except along the southern edge where a subtle increase is observed from the surface through 1.5 km. This vertical redistribution of moisture results in increased cloud cover in low and middle levels along the southern edge, while over the central and northern parts of the city, cloud cover decreases in low levels but increases in middle levels. The reduction in low-level moisture extending just north of the city further contributes to suppressed low cloud development in that region.

3.6. Influence on Convective Cell Initiation and Characteristics

The presence of the Houston urban area can significantly alter the initiation and characteristics of the convective cells through multiple pathways, including enhanced surface heating, increased roughness, and altered moisture fluxes. Higher surface temperatures and deeper boundary layers due to the UHI effect can promote low-level moisture convergence and upward motion, which can increase the likelihood of convective initiation (e.g., Niyogi et al., 2006). The complex environment can also disrupt the spatial distribution, intensity, and duration of convective cells (Z. Feng et al., 2016, 2019). In this section, we apply a convective cell tracking algorithm to model output to determine whether Houston urbanization affects convective properties. Only tracks that pass through the Houston metropolitan area and last longer than 2 hours are included.

During weakly forced conditions, the urban environment plays a strong role in triggering and intensifying convection. The Control simulation produces more convective cells, with initiation beginning around 11 LST and peaking near 15 LST, consistent with the timing of maximum surface heating (Figure 12). Urbanization increases the number of convective cells throughout the daytime and evening without substantially altering the diurnal variation of convection occurrence. The convective cells in the Control simulation are on average slightly less intense, with 1% smaller maximum reflectivity, 3% ($p < 0.05$) lower in 20 dBZ echo top height, and 2% ($p < 0.05$) smaller horizontal footprints compared to their NoUrban counterparts. However, urbanization significantly reduces the mean duration by 8% ($p < 0.05$) and distance by 16% ($p < 0.05$) (Figure 13).

During strongly forced conditions, convective cells initiate earlier in the day, beginning around 09 LST and peaking near 14 LST (Figure 12). This earlier onset, compared to weakly forced conditions, reflects large-scale meteorological forcing contributing to drive vertical ascent independent of surface thermal conditions. Convective

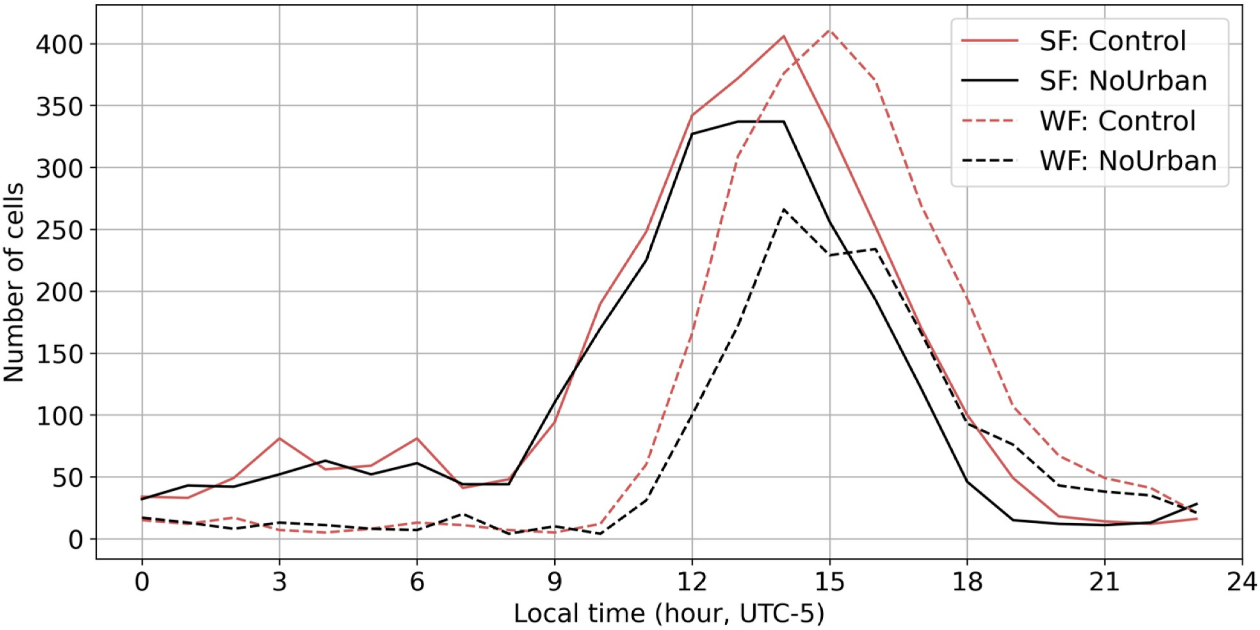

Figure 12. Diurnal distribution of convective cell counts under strongly forced and weakly forced conditions for Control and NoUrban simulations. The numbers are calculated within the white box over Houston in Figure 2c over three summers.

activity gradually diminishes by 20 LST in the Control simulation, and slightly earlier in the NoUrban simulation. Urbanization increases the number of cells during strongly forced conditions modestly in the afternoon and slightly prolongs the convective cell initiation window, with small impacts on the characteristics of cells during SFA, causing less than 2% reduction in area, reflectivity, and height (Figure 13). However, the urban land cover significantly reduces the duration and distance by 5% and 15%, respectively, which is consistent with those in WFA conditions.

Figure 14 shows the tracks of convective cells in both simulations under different large-scale environments. During WFAs, the Control simulation shows numerous short tracks densely clustered around the Houston metropolitan area, indicating localized initiation and weak propagation. Most cells form in or near the city, with a preference for initiation to the east of the urban core, and tend to drift westward or remain nearly stationary before dissipating. The NoUrban simulation also shows a similar convective activity, but with fewer initiation points in the area corresponding to the urban footprint. During SFAs, both simulations exhibit long-distance tracks, propagating primarily from south to north. While the enhanced large-scale moisture transport promotes the initiation of the cells, the urban landscape may still modulate cell structure, local distribution, and propagation. In particular, cells in the NoUrban simulation tend to travel farther north compared to those in the Control run, reflecting the additional surface drag due to urban roughness.

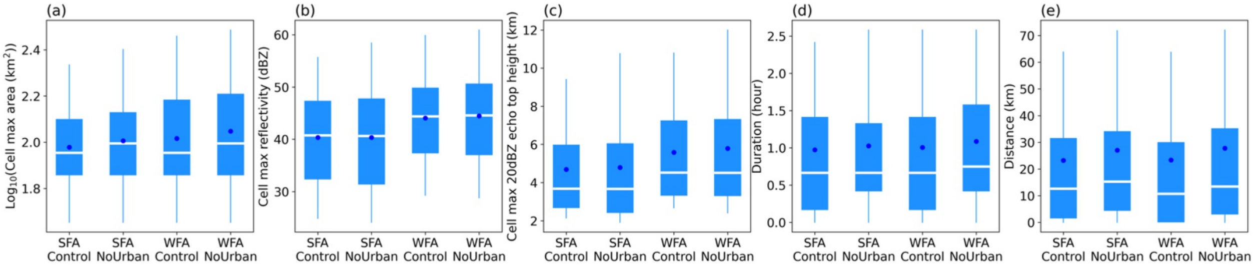

Figure 13. Boxplots of convective cell properties under strongly forced and weakly forced afternoons for both Control and NoUrban simulations. The central white line denotes the median, the box bounds indicate the interquartile range (IQR) (25th to 75th percentiles), and the whiskers extend to 1.5 times the IQR. The blue dots mark the mean values.

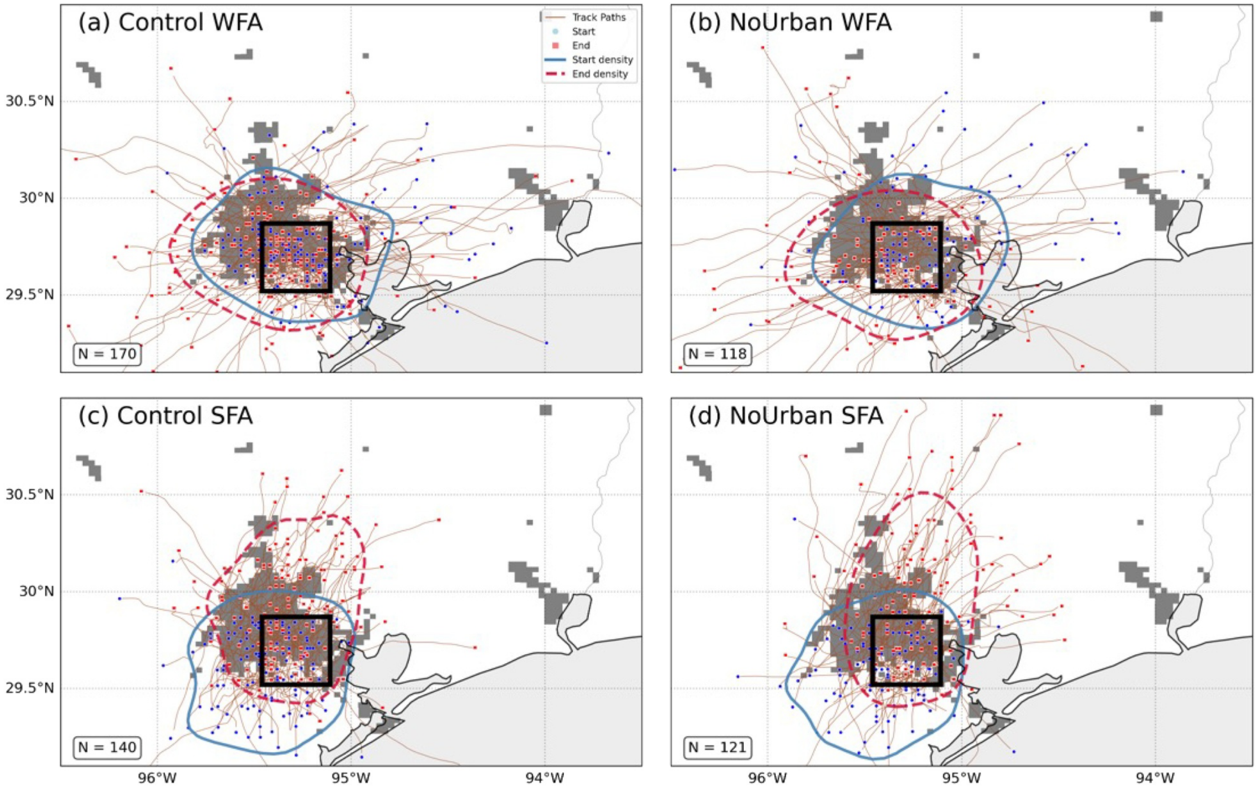

Figure 14. Tracks of convective cells in Control and NoUrban simulations under (a), (b) weakly forced afternoons (WFA) conditions and (c), (d) strongly forced afternoons (SFA) conditions. The analysis is restricted to cell tracks that pass through the urban core analysis box (black rectangle). Composite analysis showing track paths (brown lines), initiation points (blue dots), and dissipation points (red dots). Blue solid contours indicate high-density initiation regions (90th percentiles of kernel density distribution), while red dashed contours show high-density dissipation regions. Urban areas are shown in black. Sample sizes (N) indicate the number of convective tracks in each category.

3.7. Limitations and Future Improvement

While this study isolates the bulk thermodynamic and aerodynamic impacts of urban land cover, several important limitations remain. First, while 3-km grid spacing permits the grid-scale convective motions, it does not fully resolve individual convective updrafts and the dynamic entrainment associated with thermal circulations (e.g., Morrison et al., 2020). However, multi-month simulations at kilometer grid spacing well reproduce many observed characteristics (Zhang et al., 2024). It is also expensive and time consuming to conduct multi-season simulations at sub-kilometer simulations. Even at sub-kilometer grid spacing, models struggle to represent eddies driving shallow cumulus formation (e.g., Mejia et al., 2024). Accurate representation of convective cloud dynamics requires large eddy simulation (LES) with 100 m grid spacing or finer (e.g., Hong et al., 2025), albeit at significantly higher computational cost. Second, the radiation physics in our simulation is updated every 4 min, which is standard for this resolution. However, the intermittency of radiative update relative to the dynamical time step can still limit the model stability to capture rapid cloud-radiative feedbacks (Matsui et al., 2020). Third, we did not include aerosol effects, which can influence convective clouds through both radiative (e.g., Fast et al., 2006) and microphysical pathways (e.g., Varble et al., 2023). Studies have found that neglecting aerosol-cloud interactions could contribute to biases in convective intensity and rainfall, especially during pollution episodes (e.g., Fan et al., 2020). Fourth, our analysis encompasses three consecutive summers. While prior short-term simulations have successfully captured the dominance of urban heating during specific heatwave events (Mejia et al., 2024), our multi-year data set provides the necessary sample size to statistically stratify urban impact across distinct synoptic regimes and allows us to assess the flow-regime dependence of urban-cloud interaction. However, longer-term simulations would be valuable for assessing interannual variability and producing more robust statistics. Fifth, this study uses ERA5 soil moisture as the initial condition, which could introduce biased mean values and underestimated soil moisture heterogeneity. Urban-rural contrasts in soil moisture can be substantial, and biases in the soil moisture have been shown to impact the surface energy budget and land-atmosphere coupling strength (Tai et al., 2025; Yang et al., 2025). Finally, because the simulations are initialized only 3 days before the analysis period and June is used as an extended spin-up, some aspects of the soil-moisture distribution and large-scale land–atmosphere adjustment, particularly over western croplands and eastern forests, may still be evolving. Although monthly diagnostics do not show a systematic drift over June–August, the details of the domain-wide rebalancing of energy and moisture could be sensitive to both spin-up length and model domain size. Future work with longer spin-up and alternative domain configurations will be valuable to further constrain these slow adjustments.

4. Conclusions

In this study, we investigated how Houston's urban landscape modulates summertime cloud formation and convective cell characteristics under different large-scale meteorological patterns using a combination of satellite data, radar observations and convection-permitting WRF simulations. Our results reveal that Houston urbanization influences cloud evolution behavior through both aerodynamic and thermodynamic pathways, with effects that are strongly dependent on the prevailing synoptic conditions.

Satellite and radar observations show that cloud cover and convective activity are locally enhanced over Houston relative to surrounding rural areas. MODIS data indicate that the summer cloud fraction is approximately 5%–10% higher over the urban core, while radar reflectivity data reveal more frequent afternoon convective activity in the city.

Under strongly forced morning (SFM) conditions, the urban surface acts as an obstacle that slows and lifts moist southerly flow, increasing the low cloud fraction by up to 8% over the urban core and reducing it by 2%–5% downwind, forming a dipole cloud pattern mostly confined below 2 km. Cloud cover in middle levels shows minimal change. For convective clouds, under weakly forced afternoon (WFA) conditions, enhanced sensible heat flux deepens the boundary layer and generates urban-induced convergence that lifts moist rural air, increasing cloud fraction in the middle level by over 8% and promoting convective cell initiation. This finding confirms recent work identifying urban thermal forcing as the primary driver of cloud enhancement under quiescent conditions (Mejia et al., 2024).

Under strongly forced afternoon (SFA) conditions, synoptic ascent and urban influence both contribute to modulating cloud structure. The city increases cloud cover at the middle level and slightly suppresses clouds at the low level in downwind areas due to vertical moisture redistribution. A novelty of this study is the application of Lagrangian cell tracking to quantify the lifecycle of individual storms. For the WFA and SFA conditions, the urban land cover significantly increases the number of convective cells within the urban area and leads to shorter duration and travel distance of the cells, without significantly changing the area, intensity, and maximum 20 dBz echo top height. This convective cell tracking analysis offers evidence that while urbanization may alter the intensity of individual cells less drastically in this region, it significantly reshapes their lifecycle and residence time, a finding that provides a robust statistical context to prior case-study observations.

Conflict of Interest

The authors declare no conflicts of interest relevant to this study.

Availability Statement

The data sets used in this study are all publicly available. ERA5 data were downloaded from https://doi.org/10.24381/cds.adbb2d47 (Hersbach et al., 2023). The MODIS Aqua Level 2 Cloud Product is available at https://ladsweb.modaps.eosdis.nasa.gov/missions-and-measurements/products/MYD06_L2 (Platnick et al., 2015). The Level-II Radar reflectivity at the KHGX site is downloaded from https://registry.opendata.aws/noaa-nexrad. The radiosonde data were acquired from the ARM discovery website: https://adc.arm.gov//discovery/#/results/s::TRACER. The MesoWest data are downloaded from https://mesowest.utah.edu/cgi-bin/droman/site_map.cgi. The WRF code is available at https://github.com/wrf-model/WRF/releases/tag/v4.2. The PyFLEXTRKR software is available at https://github.com/FlexTRKR/PyFLEXTRKR.

Acknowledgments

This research was supported by the Atmospheric Science Research (ASR) program as part of the DOE Office of Biological and Environmental Research. This research used resources of the National Energy Research Scientific Computing Center (NERSC), a DOE User Facility (project m1657). Pacific Northwest National Laboratory is operated by DOE by the Battelle Memorial Institute under contract DE-AC05-76RL01830. We also appreciate the observational data provided by ARM.

References

Algarra, I., Eiras-Barca, J., Nieto, R., Gimeno, L., & Miguez-Macho, G. (2018). On the assessment of the moisture transport by the great plains low-level jet. Retrieved from https://scispace.com/papers/on-the-assessment-of-the-moisture-transport-by-the-great-3i08811j3w

Ashley, W. S., Bentley, M. L., & Stallins, J. A. (2012). Urban-induced thunderstorm modification in the southeast United States. *Climatic Change*, *113*(2), 481–498. https://doi.org/10.1007/s10584-011-0324-1

Barlow, J. F. (2014). Progress in observing and modelling the urban boundary layer. *Urban Climate*, *10*, 216–240. https://doi.org/10.1016/j.uclim.2014.03.011

Chakraborty, T. C., Wang, J., Qian, Y., Pringle, W., Yang, Z., & Xue, P. (2023). Urban versus Lake impacts on heat stress and its disparities in a shoreline city. *GeoHealth*, *7*(11), e2023GH000869. https://doi.org/10.1029/2023gh000869

Changnon, S. A., Jr., Huff, F. A., & Semonin, R. G. (1971). METROMEX: An investigation of inadvertent weather modification. *Bulletin of the American Meteorological Society*, *52*(10), 958–968. https://doi.org/10.1175/1520-0477(1971)052<0958:maioiw>2.0.co;2

Chen, F., & Dudhia, J. (2001). Coupling an advanced land surface–hydrology model with the penn State–NCAR MM5 modeling system. Part I: Model implementation and sensitivity. *Monthly Weather Review*, *129*(4), 569–585. https://doi.org/10.1175/1520-0493(2001)129<0569:caalsh>2.0.co;2

Chen, F., Miao, S., Tewari, M., Bao, J., & Kusaka, H. (2011). A numerical study of interactions between surface forcing and sea breeze circulations and their effects on stagnation in the greater Houston area. *Journal of Geophysical ResearchD: Atmospheres*, *116*(D12), D12105. https://doi.org/10.1029/2010jd015533

Fan, J., Zhang, Y., Li, Z., Hu, J., & Rosenfeld, D. (2020). Urbanization-induced land and aerosol impacts on sea-breeze circulation and convective precipitation. *Atmospheric Chemistry and Physics*, *20*(22), 14163–14182. https://doi.org/10.5194/acp-20-14163-2020

Fast, J. D., Gustafson, W. I., Jr., Easter, R. C., Zaveri, R. A., Barnard, J. C., Chapman, E. G., et al. (2006). Evolution of ozone, particulates, and aerosol direct radiative forcing in the vicinity of Houston using a fully coupled meteorology-chemistry-aerosol model. *Journal of Geophysical Research*, *111*(D21), D21305. https://doi.org/10.1029/2005jd006721

Feng, Z., Hardin, J., Barnes, H. C., Li, J., Leung, L. R., Varble, A., & Zhang, Z. (2023). PyFLEXTRKR: A flexible feature tracking python software for convective cloud analysis. *Geoscientific Model Development*, *16*(10), 2753–2776. https://doi.org/10.5194/gmd-16-2753-2023

Feng, Z., Houze, R. A., Leung, L. R., Song, F. F., Hardin, J. C., Wang, J. Y., et al. (2019). Spatiotemporal characteristics and large-scale environments of mesoscale convective systems east of the rocky Mountains. *Journal of Climate*, *32*(21), 7303–7328. https://doi.org/10.1175/jcli-d-19-0137.1

Feng, Z., Leung, L. R., Hagos, S., Houze, R. A., Burleyson, C. D., & Balaguru, K. (2016). More frequent intense and long-lived storms dominate the springtime trend in central US rainfall. *Nature Communications*, *7*(1), 13429. https://doi.org/10.1038/ncomms13429

Feng, Z., Varble, A., Hardin, J., Marquis, J., Hunzinger, A., Zhang, Z., & Thieman, M. (2022). Deep convection initiation, growth, and environments in the complex terrain of central Argentina during CACTI. *Monthly Weather Review*, *150*(5), 1135–1155. https://doi.org/10.1175/mwr-d-21-0237.1

Garuma, G. F. (2022). University of Quebec at Montreal (UQAM), faculty of sciences, institute of Environmental sciences, Canada, and entoto observatory and research center, atmospheric and climate science unit, department of space science and application research at the Ethiopian space science and technology institute, Addis Ababa, Ethiopia. *How the interaction of heatwaves and urban heat islands amplify urban warming. Advances in Environmental and Engineering Research*, *3*(2).

Helmus, J. J., & Collis, S. M. (2016). The python ARM radar toolkit (py-ART), a library for working with weather radar data in the python programming language. *Journal of Open Research Software*, *4*(1), 25. https://doi.org/10.5334/jors.119

Hersbach, H., Bell, B., Berrisford, P., Biavati, G., Horányi, A., Muñoz Sabater, J., et al. (2023). ERA5 hourly data on single levels from 1940 to present [Dataset]. *Copernicus Climate Change Service (C3S) Climate Data Store (CDS)*. https://doi.org/10.24381/cds.adbb2d47

Hersbach, H., Bell, B., Berrisford, P., Hirahara, S., Horányi, A., Muñoz-Sabater, J., et al. (2020). The ERA5 global reanalysis. *Quarterly Journal of the Royal Meteorological Society*, *146*(730), 1999–2049. https://doi.org/10.1002/qj.3803

Hong, C., Qu, Z., Zhang, C., Qian, J., Zhang, Y., Li, X., et al. (2025). Refinement of wrf-Bem to improve the simulation of wind-temperature-humidity in the high density urban area: A case study of megacity. https://doi.org/10.2139/ssrn.5092291

Iacono, M. J., Delamere, J. S., Mlawer, E. J., Shephard, M. W., Clough, S. A., & Collins, W. D. (2008). Radiative forcing by long-lived greenhouse gases: Calculations with the AER radiative transfer models. *Journal of Geophysical Research, D: Atmospheres*, *113*(D13), D13103. https://doi.org/10.1029/2008jd009944

Janjić, Z. I. (1990). The step-mountain coordinate: Physical package. *Monthly Weather Review*, *118*(7), 1429–1443. https://doi.org/10.1175/1520-0493(1990)118<1429:tsmcpp>2.0.co;2

Jensen, M., PNNL, B. N. L., & ANL, O. (2023). Tracking aerosol convection interactions experiment (TRACER) field campaign report. https://doi.org/10.2172/2202672

Katzfey, J., Schlünzen, K. H., & Hoffmann, P. (2024). Effects of urban areas on the diurnal cycle of temperature and precipitation in a global climate simulation. *Quarterly Journal of the Royal Meteorological Society. Royal Meteorological Society (Great Britain)*, *150*(765), 4885–4914. https://doi.org/10.1002/qj.4847

Labzovskii, L. D., Papayannis, A., Binietoglou, I., Banks, R. F., Baldasano, J. M., Toanca, F., et al. (2018). Relative humidity vertical profiling using lidar-based synergistic methods in the framework of the Hygra-CD campaign. *Annales Geophysicae*, *36*(1), 213–229. https://doi.org/10.5194/angeo-36-213-2018

Liu, J., & Niyogi, D. (2019). Meta-analysis of urbanization impact on rainfall modification. *Scientific Reports*, *9*(1), 7301. https://doi.org/10.1038/s41598-019-42494-2

Liu, Y., Qian, Y., Berg, L. K., Feng, Z., Li, J., Chen, J., & Yang, Z. (2024). Tracking precipitation features and associated large-scale environments over southeastern Texas. *Atmospheric Chemistry and Physics*, *24*(14), 8165–8181. https://doi.org/10.5194/acp-24-8165-2024

Liu, Y., Qian, Y., Feng, S., Berg, L. K., Juliano, T. W., Jiménez, P. A., & Liu, Y. (2022). Sensitivity of solar irradiance to model parameters in cloud and aerosol treatments of WRF-Solar. *Solar Energy*, *233*, 446–460. https://doi.org/10.1016/j.solener.2022.01.061

Martilli, A., Clappier, A., & Rotach, M. W. (2002). An urban surface exchange parameterisation for mesoscale models. *Boundary-Layer Meteorology*, *104*(2), 261–304. https://doi.org/10.1023/a:1016099921195

Matsui, T., Zhang, S. Q., Lang, S. E., Tao, W.-K., Ichoku, C., & Peters-Lidard, C. D. (2020). Impact of radiation frequency, precipitation radiative forcing, and radiation column aggregation on convection-permitting West African monsoon simulations. *Climate Dynamics*, *55*(1–2), 193–213. https://doi.org/10.1007/s00382-018-4187-2

Mejia, J. F., Henao, J. J., & Eslami, E. (2024). Role of clouds in the urban heat island and extreme heat: Houston-galveston metropolitan area case. *Journal of Geophysical Research: Atmospheres*, *129*(17), e2024JD041243. https://doi.org/10.1029/2024jd041243

Morrison, H., Peters, J. M., Varble, A. C., Hannah, W. M., & Giangrande, S. E. (2020). Thermal chains and entrainment in cumulus updrafts. Part I: Theoretical description. *Journal of the Atmospheric Sciences*, *77*(11), 3637–3660. https://doi.org/10.1175/jas-d-19-0243.1

Niyogi, D., Holt, T., Zhong, S., Pyle, P. C., & Basara, J. B. (2006). Urban and land surface effects on the 30 July 2003 mesoscale convective system event observed in the southern great plains. *Journal of Geophysical Research*, *111*(19), D19107. https://doi.org/10.1029/2005JD006746

Omidvar, H., Bou-Zeid, E., Li, Q., Mellado, J.-P., & Klein, P. (2020). Plume or bubble? mixed-Convection flow regimes and city-scale circulations. *Journal of Fluid Mechanics*, *897*(A5), A5. https://doi.org/10.1017/jfm.2020.360

Pielke, R. A. S. (2001). Influence of the spatial distribution of vegetation and soils on the prediction of cumulus convective rainfall. *Reviews of Geophysics*, *39*(2), 151–177. https://doi.org/10.1029/1999rg000072

Platnick, S., Ackerman, S., King, M., Meyer, K., Menzel, W., Holz, R., et al. (2015). MODIS atmosphere L2 cloud product (06_L2). NASA MODIS adaptive processing system [Dataset]. *Goddard Space Flight Center*. https://doi.org/10.5067/MODIS/MYD06_L2.061

Qian, Y., Chakraborty, T. C., Li, J., Li, D., He, C., Sarangi, C., et al. (2022). Urbanization impact on regional climate and extreme weather: Current understanding, uncertainties, and future research directions. *Advances in Atmospheric Sciences*, *39*(6), 819–860. https://doi.org/10.1007/s00376-021-1371-9

Qian, Y., Long, C. N., Wang, H., Comstock, J. M., McFarlane, S. A., & Xie, S. (2012). Evaluation of cloud fraction and its radiative effect simulated by IPCC AR4 global models against ARM surface observations. *Atmospheric Chemistry and Physics*, *12*(4), 1785–1810. https://doi.org/10.5194/acp-12-1785-2012

Rieck, M., Hohenegger, C., & van Heerwaarden, C. C. (2014). The influence of land surface heterogeneities on cloud size development. *Monthly Weather Review*, *142*(10), 3830–3846. https://doi.org/10.1175/mwr-d-13-00354.1

Salamanca, F., Krpo, A., Martilli, A., & Clappier, A. (2010). A new building energy model coupled with an urban canopy parameterization for urban climate Simulations—Part I. Formulation, verification, and sensitivity analysis of the model. *Theoretical and Applied Climatology*, *99*(3–4), 331–344. https://doi.org/10.1007/s00704-009-0142-9

Shepherd, J. M. (2005). A review of current investigations of urban-induced rainfall and recommendations for the future. *Earth Interactions*, *9*(12), 1–27. https://doi.org/10.1175/ei156.1

Skamarock, W. C., Klemp, J. B., Dudhia, J., Gill, D. O., Liu, Z., Berner, J., et al. (2019). *A description of the advanced research WRF model version 4*. UCAR/NCAR. https://doi.org/10.5065/1DFH-6P97

Song, F., Feng, Z., Leung, L. R., Jr., Houze, R. A., Wang, J., Hardin, J., & Homeyer, C. R. (2019). Contrasting spring and summer large-scale environments associated with mesoscale convective systems over the U.S. great plains contrasting spring and summer large-scale environments associated with mesoscale convective systems over the U.S. great plains. *Journal of Climate*, *32*(20), 6749–6767. https://doi.org/10.1175/jcli-d-18-0839.1

Steiner, M., Houze, R. A., Jr., & Yuter, S. E. (1995). Climatological characterization of three-dimensional storm structure from operational radar and rain gauge data. *Journal of Applied Meteorology*, *34*(9), 1978–2007. https://doi.org/10.1175/1520-0450(1995)034⟨1978:ccotds⟩2.0.co;2

Tai, S.-L., Yang, Z., Gaudet, B., Sakaguchi, K., Berg, L., Kaul, C., et al. (2025). A 1 km soil moisture data over eastern CONUS generated through assimilating SMAP data into the Noah-MP land surface model. *Earth System Science Data Discussions*. https://doi.org/10.5194/essd-2024-599

Theeuwes, N. E., Barlow, J. F., Teuling, A. J., Grimmond, C. S. B., & Kotthaus, S. (2019). Persistent cloud cover over mega-cities linked to surface heat release. *npj Climate and Atmospheric Science*, *2*(1), 15. https://doi.org/10.1038/s41612-019-0072-x

Theeuwes, N. E., Boutle, I. A., Clark, P. A., & Grimmond, S. (2022). Understanding London's summertime cloud cover. *Quarterly Journal of the Royal Meteorological Society*, *148*(742), 454–465. https://doi.org/10.1002/qj.4214

Thompson, G., Field, P. R., Rasmussen, R. M., & Hall, W. D. (2008). Explicit forecasts of winter precipitation using an improved bulk microphysics scheme. Part II: Implementation of a new snow parameterization. *Monthly Weather Review*, *136*(12), 5095–5115. https://doi.org/10.1175/2008mwr2387.1

Thompson, G., Rasmussen, R. M., & Manning, K. (2004). Explicit forecasts of winter precipitation using an improved bulk microphysics scheme. Part I: Description and sensitivity analysis. *Monthly Weather Review*, *132*(2), 519–542. https://doi.org/10.1175/1520-0493(2004)132<0519:efowpu>2.0.co;2

Tymvios, F., Charalambous, D., Michaelides, S., & Lelieveld, J. (2018). Intercomparison of boundary layer parameterizations for summer conditions in the eastern mediterranean island of Cyprus using the WRF - ARW model. *Atmospheric Research*, *208*, 45–59. https://doi.org/10.1016/j.atmosres.2017.09.011

Varble, A. C., Igel, A. L., Morrison, H., Grabowski, W. W., & Lebo, Z. J. (2023). Opinion: A critical evaluation of the evidence for aerosol invigoration of deep convection. *Atmospheric Chemistry and Physics*, *23*(21), 13791–13808. https://doi.org/10.5194/acp-23-13791-2023

Vesanto, J., & Alhoniemi, E. (2000). Clustering of the self-organizing map. *IEEE Transactions on Neural Networks / a Publication of the IEEE Neural Networks Council*, *11*(3), 586–600. https://doi.org/10.1109/72.846731

Vo, T. T., Hu, L., Xue, L., Li, Q., & Chen, S. (2023). Urban effects on local cloud patterns. *Proceedings of the National Academy of Sciences of the United States of America*, *120*(21), e2216765120. https://doi.org/10.1073/pnas.2216765120

Wang, D., Jensen, M. P., Taylor, D., Kowalski, G., Hogan, M., Wittemann, B. M., et al. (2022). Linking synoptic patterns to cloud properties and local circulations over southeastern Texas. *Journal of Geophysical ResearchD: Atmospheres*, *127*(5), e2021JD035920. https://doi.org/10.1029/2021jd035920

Whiteman, C. D., Bian, X. D., & Zhong, S. Y. (1997). Low-level jet climatology from enhanced rawinsonde observations at a site in the southern great plains. *Journal of Applied Meteorology*, *36*(10), 1363–1376. https://doi.org/10.1175/1520-0450(1997)036<1363:lljcfe>2.0.co;2

Wu, Y., & Raman, S. (1996). The great plains low-level jet (LLJ) during the atmospheric radiation measurement (ARM) intensive observation period (IOP)-4 and simulations of land use pattern effect on the LLJ. Retrieved from https://scispace.com/papers/the-great-plains-low-level-jet-llj-during-the-atmospheric-2pequ9b290

Xu, K.-M., & Randall, D. A. (1996). A semiempirical cloudiness parameterization for use in climate models. *Journal of the Atmospheric Sciences*, *53*(21), 3084–3102. https://doi.org/10.1175/1520-0469(1996)053<3084:ascpfu>2.0.co;2

Yang, Z., Niu, G.-Y., Qian, Y., Berg, L. K., Fast, J., Kaul, C. M., et al. (2025). Improved representations of land-atmosphere interactions over the Continental U.s. through dynamic root modeling. *Journal of Advances in Modeling Earth Systems*, *17*(7), e2024MS004474. https://doi.org/10.1029/2024ms004474

Zhang, H., Wu, C., Chen, W., & Huang, G. (2019). Effect of urban expansion on summer rainfall in the pearl river Delta, south China. *Journal of Hydrology*, *568*, 747–757. https://doi.org/10.1016/j.jhydrol.2018.11.036

Zhang, W., Villarini, G., Vecchi, G. A., & Smith, J. A. (2018). Urbanization exacerbated the rainfall and flooding caused by hurricane harvey in Houston. *Nature*, *563*(7731), 384–388. https://doi.org/10.1038/s41586-018-0676-z

Zhang, Z., Varble, A. C., Feng, Z., Marquis, J. N., Hardin, J. C., & Zipser, E. J. (2024). Dependencies of simulated convective cell and system growth biases on atmospheric instability and model resolution. *Journal of Geophysical Research. Atmospheres: JGR*, *129*(22), e2024JD041090. https://doi.org/10.1029/2024jd041090